

The Local Volume HI Survey: star formation properties

Jing Wang^{1,2*}, Bärbel S. Koribalski^{1†}, Tom H. Jarrett³, Peter Kamphuis⁴, Zhao-Yu Li^{5,6},
Luis C. Ho^{2,7}, Tobias Westmeier⁸, Li Shao¹, Claudia del P. Lagos^{8,9}, O. Ivy Wong^{8,9},
Paolo Serra¹⁰, Lister Staveley-Smith^{8,9}, Gyula Józsa^{11,12,13}, Thijs van der Hulst¹⁴

Á.R. López-Sánchez^{15,16}

¹ Australia Telescope National Facility, CSIRO Astronomy and Space Science, PO box 76, Epping, NSW 1710, Australia

² Kavli Institute for Astronomy and Astrophysics, Peking University, Beijing 100871, China

³ Department of Astronomy, University of Cape Town, Private Bag X3, Rondebosch, 7701, South Africa

⁴ National Centre for Radio Astrophysics, TIFR, Ganeshkhind, Pune 411007, India

⁵ Key Laboratory for Research in Galaxies and Cosmology, Shanghai Astronomical Observatory, Chinese Academy of Sciences, 80 Nandan Road, Shanghai 200030, China

⁶ College of Astronomy and Space Sciences, University of Chinese Academy of Sciences, 19A Yuquan Road, Beijing 100049, China

⁷ Department of Astronomy, School of Physics, Peking University, Beijing 100871, China

⁸ International Centre for Radio Astronomy Research (ICRAR), M468, University of Western Australia, 35 Stirling Hwy, Crawley, WA 6009, Australia

⁹ ARC Centre of Excellence for All-Sky Astrophysics (CAASTRO), Australia

¹⁰ INAF - Osservatorio Astronomico di Cagliari, Via della Scienza 5, I-09047 Selargius (CA), Italy

¹¹ SKA South Africa Radio Astronomy Research Group, 3rd Floor, The Park, Park Road, Pinelands, 7405, South Africa

¹² Rhodes University, Department of Physics and Electronics, Rhodes Centre for Radio Astronomy Techniques & Technologies, PO Box 94, Grahamstown, 6140, South Africa

¹³ Argelander-Institut für Astronomie, Auf dem Hügel 71, D-53121 Bonn, Germany

¹⁴ University of Groningen, Kapteyn Astronomical Institute, Landleven 12, 9747 AD, Groningen, The Netherlands

¹⁵ Australian Astronomical Observatory, PO Box 915, North Ryde, NSW 1670, Australia

¹⁶ Department of Physics and Astronomy, Macquarie University, NSW 2109, Australia

Accepted 2017 ???? ?? Received 2017 ???? ??; in original form 2017 January

ABSTRACT

We built a multi-wavelength dataset for galaxies from the Local Volume HI Survey (LVHIS), which comprises 82 galaxies. We also select a sub-sample of ten large galaxies for investigating properties in the galactic outskirts. The LVHIS sample covers nearly four orders of magnitude in stellar mass and two orders of magnitude in HI mass fraction (f_{HI}). The radial distribution of HI gas with respect to the stellar disc is correlated with f_{HI} but with a large scatter. We confirm the previously found correlations between the total HI mass and star formation rate (SFR), and between HI surface densities and SFR surface densities beyond R_{25} . However, the former correlation becomes much weaker when the average surface densities rather than total mass or rate are considered, and the latter correlation also becomes much weaker when the effect of stellar mass is removed or controlled. Hence the link between SFR and HI is intrinsically weak in these regions, consistent with what was found on kpc scales in the galactic inner regions. We find a strong correlation between the SFR surface density and the stellar mass surface density, which is consistent with the star formation models where the gas is in quasi-equilibrium with the mid-plane pressure. We find no evidence for HI warps to be linked with decreasing star forming efficiencies.

Key words: interstellar medium, spiral galaxies, star formation

* Email: hyacinthwj@gmail.com

† Email: Baerbel.Koribalski@csiro.au

1 INTRODUCTION

How galaxies evolve in their stellar population is a key question in galactic astronomy, and the properties of atomic hydrogen HI gas contain key information to that question. The star formation rates (SFR) and stellar masses of star forming galaxies are observed to correlate with each other and this relationship is often referred to as the star formation ‘main sequence’ (MS, Noeske et al. 2007; Elbaz et al. 2007; Dutton et al. 2010). The star formation quenching or quenched galaxies lie below the sequence with a wide range of star formation rates (Whitaker et al. 2012). The deviation to the median SFR of the MS at a fixed stellar mass strongly depends on the HI gas fraction of galaxies (Saintonge et al. 2016). Hence the quenching of star formation is accompanied by removal or exhaustion of HI gas. This is because HI forms the initial reservoir from which molecular gas and subsequently, stars are formed. In order to better understand galaxy quenching, we first need to understand how HI fuels star formation, i.e. the relation between HI and SFR in star-forming galaxies.

Several large single-dish HI surveys have been carried out in the past decade. The shallow blind surveys, ALFALFA (Arecibo Legacy Fast ALFA, Giovanelli et al. 2005) and HIPASS (HI Parkes All-Sky Survey, Meyer et al. 2004; Koribalski et al. 2004), and the targeted, optically selected, GASS survey (GALEX Arecibo SDSS Survey, Catinella et al. 2010) have significantly advanced our understanding of the SFR-HI relations on the global scales. Among the most interesting findings are, 1) SFR and HI mass are tightly correlated for the ALFALFA sample whose galaxies are mostly on the star-forming sequence (Huang et al. 2012a); 2) the star forming efficiencies (SFE=SFR/ M_{HI}) in the HI-selected ALFALFA sample are on average three times lower than those in the optically selected GASS sample, which includes both star-forming and transitional galaxies (Huang et al. 2012a; Schiminovich et al. 2010); 3) there is a weak correlation between SFE and stellar mass in the ALFALFA sample (Huang et al. 2012a), which was not found within the GASS sample (Schiminovich et al. 2010), possibly due to the small range in stellar masses for GASS and/or the different sample selections; 4) there is a weak correlation between SFE and optical surface brightness for galaxies selected from the HIPASS sample (Wong et al. 2016).

The strong correlation between SFR and HI mass found on global scales seems to be at odds with the lack of correlation between surface densities of SFR and HI found on sub-kpc scales in the inner parts of galaxies (Bigiel et al. 2008). The latter is contrasted by the tight scaling relation between surface densities of SFR and molecular gas (Bigiel et al. 2008), and the explanation is that the molecular gas clouds rather than the HI gas directly form stars. This difference in HI-SFR relations on kpc and global scales might be caused by the difference in scales, but can also possibly indicate different physics working on these two scales. Especially we need to keep in mind that a large fraction of the HI gas in HI-rich galaxies is distributed beyond the stellar disc where the SFE is so much lower than that in the inner disc that it would take several times the Hubble time to deplete the HI gas there (Bigiel et al. 2010).

On the other hand, the global HI-SFR correlation is present on kpc-scales in the HI dominated regions, i.e., in

irregular galaxies (Roychowdhury et al. 2014) and the outskirts of spiral and early-type galaxies (Koribalski & López-Sánchez 2009; Bigiel et al. 2010; Yim & van der Hulst 2016; Yıldız et al. 2017). However there is large scatter (~ 1.5 dex) in these relations (Roychowdhury et al. 2014; Bigiel et al. 2010). Hunter et al. (1998) showed that in irregular galaxies the SFR radial profiles actually follow the shape of stellar mass profiles better than that of HI profiles. This makes us wonder whether the same behaviour can be found in the outskirts of spiral galaxies. A possibility that could explain these trends is that both the SFR and the HI surface densities are correlated with the stellar mass surface densities in the outer regions of galaxies. The mid-plane pressure model has been commonly used to explain the link between mass surface densities and SFR (Leroy et al. 2008; Ostriker et al. 2010, e.g.), however one significant limitation is that it doesn’t explain the stochastic behaviour of star formation in these low gas density regions (Gerola et al. 1980; Teich et al. 2016).

Mass surface density is not the only possible parameter that regulates SFR. Yim & van der Hulst (2016) found that disturbances from the external environment seem to hardly affect the radial HI SFE of galaxies. On the other hand, the HI disc internal structures may affect SFE in the galactic outskirts. As demonstrated nicely in van der Kruit (2007), HI warps usually start near the optical truncation radius where the optical discs abruptly and steeply turn fainter (also see Józsa 2007; García-Ruiz et al. 2002; Briggs 1990). One possible explanation is that the HI gas in a warp has an external origin and was accreted with an angular momentum mis-aligned with that of the main disc. Conversely, the existence of an HI warp may affect the radial distribution of SFR, which is adopted in some theoretical models to explain the optical truncation radius. For example, in the model of Sánchez-Blázquez et al. (2009) the gas near a warp would have low volume densities due to the warp, and hence could not efficiently form stars. As a result a large fraction of stars beyond the warp radius were not formed in situ but rather migrated from the inner part of the galaxy disc. These theories add complexities to the HI-SFR relationship in the galactic outskirts. However, the influence of HI warps on localised SF has never been investigated statistically with observational data.

We have reviewed the apparently different behaviours of HI-SFR relations on different scales and in different regions. However, to understand them in a consistent picture has been difficult, largely due to the lack of proper datasets. The single-dish HI data spatially resolve very few galaxies while HI interferometric samples usually lack homogeneity in galaxy selection. Another common problem with HI interferometry is that extended emission of objects with large angular scales (typically > 15 arcmin) is not properly measured because there are no baselines short enough to sample such angular scales. This affects the surface densities of all extended emission, especially on the outer parts. The Local Volume HI Survey (LVHIS¹, Koribalski et al. in prep, Paper I hereafter) tends to overcome these difficulties. It is close to a volume limited HI sample of galaxies beyond the Milky

¹ <http://www.atnf.csiro.au/people/Baerbel.Koribalski/LVHIS/LVHIS-galaxies.html>

Way, built on the single-dish blind survey HIPASS (Meyer et al. 2004), by targeting all detections with a declination less than or similar to -30 degree and a distance less than 8 Mpc from the HIPASS catalogs (Meyer et al. 2004; Koribalski et al. 2004). Special care has been taken to address the missing flux problem by using compact array configurations. We also combine the interferometric data with single-dish imaging mosaics (from the Parkes Galactic All Sky Survey, GASS, McClure-Griffiths et al. 2009) to produce the HI image for the galaxy NGC 300, for which ATCA data alone is not sufficient to sample the extended HI structures (see Paper I and Stanimirovic 2002, for a description of such techniques). LVHIS hence provides us a suitable laboratory for coherently understanding the different HI-SFR relations.

This paper presents the multi-wavelength dataset for the LVHIS sample. As a first application of the dataset it investigates HI-SFR relations on global scales and in the outskirts, with the goal of reconciling the seeming contradictions of these relations from the relation observed in galactic inner regions.

The paper is organised as follows. In Section 2.1 we introduce the data used in this paper, including a brief description about the LVHIS sample and HI data. In Section 3 we analyse the multi-wavelength data for the whole LVHIS sample while in Section 4 we focus on a sub-sample of ten large LVHIS galaxies. A comparison of LVHIS with other HI surveys can be found in Section 5.1 compares LVHIS. In Section 5.2 we study the dependence of HI radial distributions on stellar properties. In Section 6 we use resolved HI properties to explore causes for the global star formation relations. In Section 7 we investigate relations between SFR, HI and stellar surface densities in the galactic outskirts. In Section 8 we search for possible links between the onset of an HI warp and the radial change of SFE. In Section 9 we summarise the paper.

Throughout this paper, we assume a Kroupa IMF (initial mass function, Kroupa 2001), and a Λ CDM cosmology with $\Omega_m = 0.3$, $\Omega_{\Lambda} = 0.7$ and $h = 0.7$. Any quantities and trends taken from the literature are converted to be consistent with these assumptions before used in this paper. Because this paper extensively discusses correlations, we define here that a strong correlation should have Pearson correlation coefficient $\rho > 0.8$, a significant correlation should have ρ between 0.6 and 0.8, a weak/moderate correlation should have ρ between 0.2 and 0.6, while no correlation corresponds to $\rho < 0.2$. Errors for correlation coefficients are calculated through bootstrapping.

2 DATA

2.1 Sample and ATCA HI data

The Local Volume HI Survey (LVHIS, Koribalski et al. in prep, Paper I) consists of a complete sample of 82 nearby galaxies ($D < 10$ Mpc) with a declination $\delta \lesssim -30^\circ$ selected from HIPASS (Meyer et al. 2004; Koribalski et al. 2004).

Using the Australia Telescope Compact Array (ATCA), sensitive HI spectral line and 20-cm radio continuum data were obtained for all LVHIS galaxies. Large galaxies like M83, NGC 3621, Circinus and others were mosaiced to ensure that the extended HI emission of the outer disc was not

missed. Paper I presents the LVHIS HI galaxy atlas (cubes and moment maps), based on the ‘natural’ weighted uv -data, and focused on the large-scale HI emission in and around the selected galaxies. Typical angular resolution is $B_{\text{maj}} \gtrsim 40''$ (ie. ~ 1 kpc at $D = 5$ Mpc), where B_{maj} is the major axis of the synthesized beam. The typical r.m.s. sensitivity is ~ 1.5 mJy beam $^{-1}$ per 4 km/s channel, which corresponds to a 5 r.m.s column density limit of 0.46×10^{20} cm $^{-2}$ assuming a 20 km/s line width. This paper makes use of the primary beam corrected cubes and moment 0 images to derive HI related properties.

Results based on the LVHIS dataset have been presented in a series of publications, including Koribalski & López-Sánchez (2009); van Eymeren et al. (2010); López-Sánchez et al. (2012); Kirby et al. (2012); Kamphuis et al. (2015); Johnson et al. (2015) and Wang et al. (2016). A parallel study of the 20-cm radio continuum emission of the sample will be presented in Shao et al. (in prep). We take R_{25} (the semi-major axis of the 25 mag arcsec $^{-2}$ isophote in the B -band) from the surface photometry catalogue of the ESO-Uppsala galaxies (Lauberts & Valentijn 1989), and the HI surface density radial profiles and R_{HI} (the semi-major axis for the HI 1 M_\odot pc $^{-2}$ isophote) from Wang et al. (2016).

The LVHIS galaxy names along with some of their key properties derived throughout this paper are listed in Table 1. The table columns are as follows: (1) LVHIS ID, (2) HIPASS name, (3) galaxyname, (4) star formation rate ($\text{SFR} = \text{SFR}_{\text{FUV}} + \text{SFR}_{\text{W4}}$; Section 3.3.2), (5) stellar mass (M_*) derived from WISE luminosities (Section 3.3.1), (6) HI fraction ($f_{\text{HI}} = M_{\text{HI}}/M_*$), (7) ratio of HI to optical radii, (8) the averaged stellar surface densities within the W1 effective radius ($\Sigma_{*,\text{eff}}$, Section 3.2), (9) the averaged SFR surface density within R_{25} ($\Sigma_{\text{SFR},r < R_{25}}$, Section 4.2.3), (10) the averaged HI surface densities within R_{25} , (11) the averaged HI surface densities within $3.2 r_s$ of the W1 band (Section 3.2). Properties in Columns 7, 10 and 11 are obtained only when the relevant radii are resolved in HI ($> b_{\text{maj}}$). The tables presented in this paper have the same order as in Paper I and Shao et al. (in prep) and we also use ‘ID’ to denote the index (starting from 1). Figure 1 shows an example multi-wavelength image of one of the 82 LVHIS galaxies.

From the LVHIS sample we also select a sub-sample of large galaxies for detailed multi-wavelength analysis (marked with l in Table 1). These, in total ten galaxies, are all the LVHIS galaxies that have an optical diameter, D_{25} , at least four times larger than the HI angular resolution and have GALEX FUV data available (Section 2.2). They include seven galaxies with Hubble types ranging between Sc and Sd, two Sm galaxies and one irregular dwarf galaxy. An atlas of these galaxies can be found in Appendix B. The HI discs are 15 to 73 times larger than the HI angular resolution. We obtain multi-wavelength radial profiles and tilted-ring HI models for this subsample in Section 4.

We note that for analysis based on this sub-sample, we use the natural weighted HI image from THINGS (The HI Nearby Galaxy Survey Walter et al. 2008) instead of the ATCA HI image for the galaxy NGC 7793. This is because for NGC 7793, the THINGS HI data have much better resolution (~ 15.6 arcsec) than the ATCA HI data (~ 364 arcsec) while they do not significantly miss flux (its HI flux 12% less than the HIPASS HI flux, comparable to the $1\sigma = 15\%$ dif-

ference between ATCA and HIPASS fluxes for LVHIS, see Paper I) due to the lack of short baselines.

2.2 GALEX

The Galaxy Evolution Explorer (Martin et al. 2005, GALEX) provides near-ultraviolet (NUV, effective wavelength $\lambda \sim 1528\text{\AA}$) and far-ultraviolet (FUV, $\lambda \sim 2271\text{\AA}$) images over a large fraction of the sky. Each image has a pixel size of $1''.5$, and the typical full width half maximum (FWHM) of the PSF (point spread function) is $5''.0$ (FUV) and $5''.5$ (NUV). The provided magnitude zero-points are calibrated in the AB mag-system. Of the 82 LVHIS galaxies, 56 are covered by the GALEX imaging survey (data release 6+7) in the NUV band and 46 in the FUV band. The remaining 26 galaxies are missing because GALEX avoided the sky near the Galactic Plane.

The depth of the available GALEX images varies substantially: 22 galaxies have relatively deep images from the Medium Imaging Survey (MIS), with typical exposure times of $t_{\text{exp}} > 1500\text{ s}$ and a depth of 22.6 mag in FUV, 9 have ultra deep images from the Deep Imaging Survey (DIS), with $t_{\text{exp}} > 10,000\text{ s}$ and a depth of 24.2 mag in FUV, while 15 have short exposures from the All-Sky Imaging Survey (AIS), with $t_{\text{exp}} \sim 100\text{ s}$ and a depth of 20 mag in FUV.

2.3 WISE

The Wide-field Infrared Survey Explorer (Wright et al. 2010, WISE) has mapped the whole sky in the 3.4, 4.6, 12 and $22\ \mu\text{m}$ MIR (mid-infrared) bands, commonly referred to as W1, W2, W3 and W4. We make use of specially constructed WISE mosaics produced with ICORE Masci (2013, Image Co-addition with optional Resolution Enhancement) as described in Cluver et al. (2014). These mosaics notably improve the angular resolution by $\sim 30\%$ from the ALLWISE images (Cutri et al. 2012) published in the WISE public release archive, which were optimised for detecting point sources. They have a pixel size of $1''$ and a resolution of $5''.9$, $6''.5$, $7''.0$ and $12''.4$ for the four bands, respectively. The typical sky rms (1σ) is 23.0, 21.8, 18.1 and 15.8 mag arcsec $^{-2}$ (Jarrett et al. 2012). The magnitude zero-points are calibrated in the Vega mag system.

2.4 Other data

Past studies have provided photometric data for several LVHIS galaxies. A comprehensive overview of the complementary datasets is given in Table 1 of Paper I. Here we review a few datasets that are used for analysis or comparison in this paper.

As part of the Local Volume Legacy (LVL) project (Kennicutt et al. 2008; Dale et al. 2009), Lee et al. (2011) obtained asymptotic fluxes (a measure of the total flux, see Section 3.1) in the GALEX bands for 390 local volume galaxies including 53 LVHIS galaxies. We will use this dataset to validate our GALEX flux measurements (Section 3.1).

The Carnegie-Irvine Galaxy Survey (Ho et al. 2011, CGS) provides B , V , R and I -band images for the 605 optically brightest galaxies in the southern sky, including 22 LVHIS galaxies. The field of view for each image is $8'.9 \times 8'.9$,

and the typical seeing is $1''$. The details are described in Ho et al. (2011) and Li et al. (2011). The survey also provides a comprehensive set of photometric measurements including total fluxes, sizes, and radial surface brightness (SB) profiles. We will use this dataset to compare with our stellar mass (M_*) estimate for the high-mass galaxies (Section 3.3).

Kirby et al. (2012) obtained deep H -band ($1.65\ \mu\text{m}$) images with the 3.9-m Anglo Australian Telescope (AAT) and performed photometry for 57 galaxies in the Local Volume. Young et al. (2014) followed up another 40 dwarf galaxies. The field of view for each image is $7'.7 \times 7'.7$, and the typical seeing is $1''.3$. The two samples combined include 37 LVHIS galaxies. We will use this dataset to compare with our stellar mass (M_*) estimate for the low-mass galaxies (Section 3.3).

The SINGG (Survey for Ionization in Neutral Gas Galaxies, Meurer et al. 2006) obtained $H\alpha$ and R -band images for 468 galaxies randomly selected from the HIPASS catalogues to uniformly sample the H I mass function. Its sister survey, SUNGG (Survey of Ultraviolet emission in Neutral-Gas Galaxies, Wong et al. 2016) used GALEX to image a subset of SINGG galaxies in the FUV and NUV bands. SINGG (SUNGG) have 19 (6) galaxies in overlap with LVHIS. We will compare our SFR and M_* estimates with those obtained in the SINGG studies (Section 3.3).

Lee et al. (2009) estimated SFRs for 300 local galaxies using data from the 11 Mpc $H\alpha$ and Ultraviolet Galaxy Survey (11HUGS). There are 29 galaxies in common for 11HUGS and LVHIS. We will compare our SFR estimates with those from Lee et al. (2009) for validation (Section 3.3).

3 ANALYSIS FOR LVHIS GALAXIES

In this section, we describe how we compute the total and radial distribution of fluxes from the WISE and GALEX images. We convert these measurements into physical properties and compare them to literature data.

3.1 GALEX photometry

We use the same pipeline described briefly in Overzier et al. (2011) to obtain photometric measurements for the LVHIS galaxies. Here we describe each step of the procedure:

(i) Global background estimate and neighbour masking. We use SExtractor (Bertin & Arnouts 1996) to produce a segmentation map for each image, where the pixels for all detected sources are labelled. We then exclude the pixels belonging to detected sources and calculate a global background value. Next we manually set this background value as input and run SExtractor again. Finally, we use the new segmentation map to mask sources around our galaxies.

(ii) Foreground star removal. For galaxies with available FUV images, we convolve these to match the slightly poorer resolution of the NUV images. Pixels associated with foreground stars are identified as having flux ratios $\text{NUV}/\text{FUV} > 5$ and NUV signal-to-noise (S/N) > 2 . For galaxies without FUV images, we inspect the NUV images and manually identify pixels containing bright point sources². We replace

² Masking foreground stars through visual inspection is subject to uncertainties, but generally speaking pixels associated with

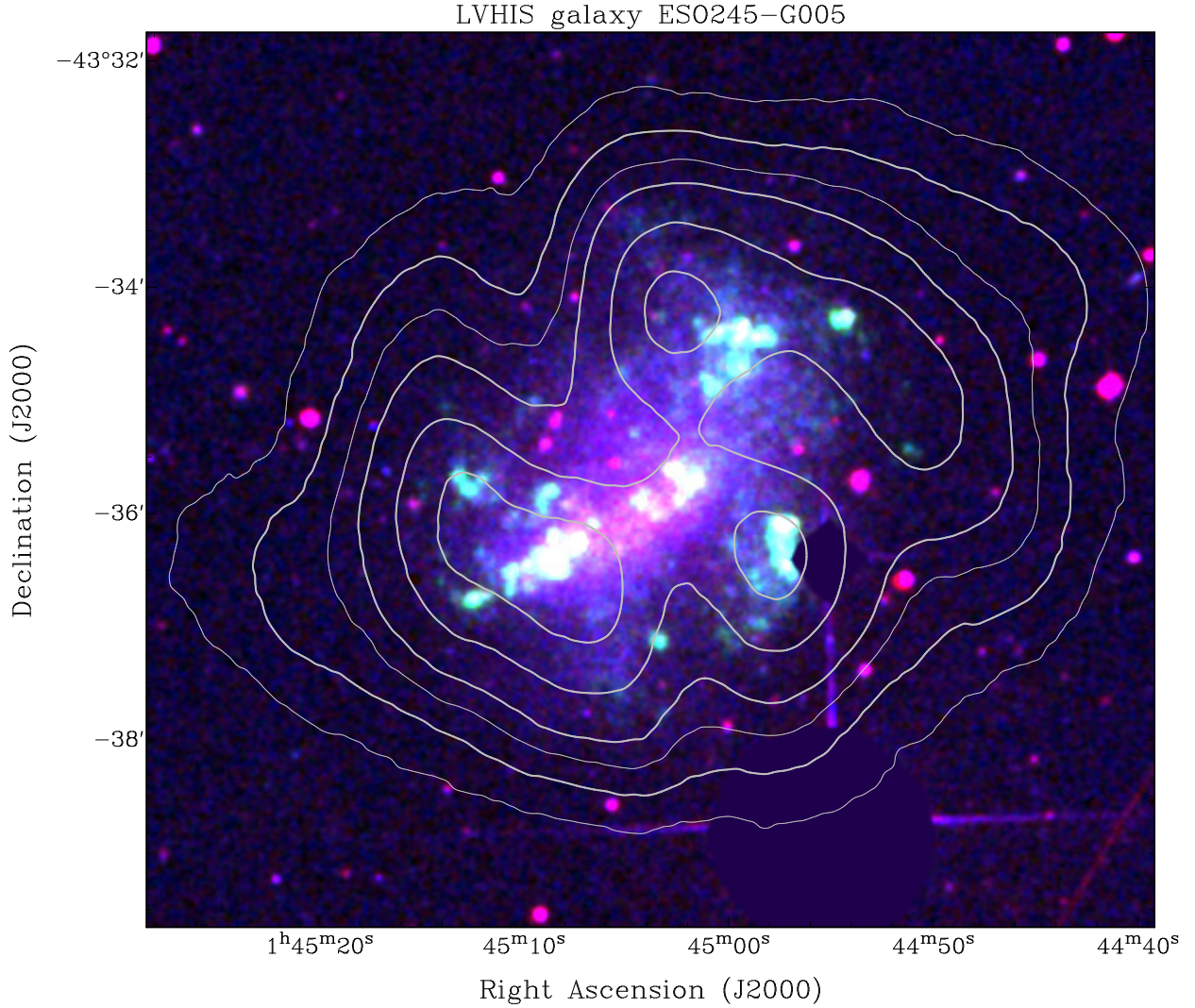


Figure 1. Multi-wavelength image of the galaxy ESO245-G005, one of 82 nearby galaxies in the Local Volume HI Survey (LVHIS, Koribalski et al. in prep). The 3-colour composite consists of DSS2 *R*-band (red), GALEX FUV (green) and DSS2 *B*-band (blue) images overlaid with ATCA HI intensity contours at 0.5, 1, 1.5, 2, 3 and 4 Jy/beam km/s. The optical and UV images were smoothed, and we masked two foreground stars.

the pixels associated with foreground stars with pixels on the other side of the galaxy centre, or the average of pixels on the galaxy isophote, depending on whether or not the pixels on the other side are also associated with foreground stars. This step makes a clean image that will also be used in the resolution matched photometric analysis (Section 4.1).

(iii) Radial profiles and residual background removal. We measure the radial profile of surface brightness (SB) along elliptical rings with a width of at least 1 pixel ($\sim 1/3$ of the PSF size). For large galaxies, the spacing is increased to sample the radial profile with at most 50 data points. The ellipticity and position angle of the rings are fixed at the optical values of the 25 mag arcsec $^{-2}$ isophote. The SB is calculated as the 3-sigma clipped mean of the distribution

foreground stars identified from the NUV/FUV values are a small fraction ($< 0.02\%$) of all the pixels. Errors introduced in the NUV fluxes through this step do not affect the science analysis (which uses the FUV but not the NUV fluxes) in this paper.

of the pixel values in each elliptical ring. We identify the radius where the profile flattens within the noise, and use the annulus between one and 1.4 times this radius around the galaxy centre to estimate a local residual of the background. We remove this residual background and cut the radial profile at a S/N of 1.25 (equivalent to an SB error of 0.87 mag).

(iv) Growth curve and total flux. We measure the growth curve (GC) of flux enclosed by elliptical apertures out to 1.25 times the last radial point of the SB radial profile. We use the GC to obtain the asymptotic flux. Following the method outlined in Lee et al. (2011), we extrapolate the relation between the derivative of the GC and the GC, and the intercept is taken as the asymptotic flux. The error of the asymptotic flux is a combination of the photometric error and error from the extrapolation. We further add a zero-point error of 0.05 mag for FUV and 0.027 mag for NUV (Morrissey et al. 2007). The asymptotic flux is taken as the total flux for GALEX bands in this paper.

Figure 2 shows the intermediate products of this pipeline for two galaxies, one is bright and with deep imaging and the other is faint and with shallow imaging. We are able to reliably measure total fluxes (with an error less than 0.5 mag) for 44 and 54 galaxies in the FUV and NUV bands, respectively. We present these photometric measurements in Table A1).

There are alternative methods to obtain the total fluxes. As adopted by Huang et al. (2012a), fitting models (e.g. exponential functions) to SB radial profiles and extrapolating helps recover faint fluxes lower than the noise level, which is especially useful for low SB dwarf galaxies. Although the majority of the LVHIS sample are dwarf galaxies, we have chosen to use the asymptotic fluxes instead of the model fluxes. This is because nearly half of the LVHIS sample only have shallow AIS images (see Section 2.2) while Huang et al. (2012a) selected galaxies with GALEX images of at least MIS-depth. Model fitting could be unreliable on our shallow images. To demonstrate the reason for our choice, in Figure 3, we test the stabilities of the two methods on images of different depths. We take the DIS FUV image (with $t_{exp} = 12987.6$ s) of NGC 300 and pretend to observe it again with shorter t_{exp} , i.e. by adding Poissonian noise to the counts. It is clear that when $t_{exp} < 1000$ s (typical for AIS), model fluxes have large uncertainties and systematic uncertainties while asymptotic fluxes are much more stable.

As an external validation, we compare our asymptotic flux measurements with those from Lee et al. (2011) for the galaxies included in both studies (53 in total). GALEX magnitudes before data release 6 as presented in Lee et al. (2011) are 0.045 mag brighter in NUV and 0.033 mag brighter in FUV as compared to the most recent releases, due to a less accurate zero-point calibration. We have corrected for this effect before the comparison. As can be seen in Figure 3.1, the LVHIS and LVL measurements of FUV fluxes agree reasonably well, with a median value and scatter of 0.085 and 0.089 mag for the differences between the two. We have reviewed our photometry steps for the outliers in the comparison, and make sure that there are no obvious errors in our processing.

3.2 WISE photometry

We use the same pipeline outlined in detail in Jarrett et al. (2016, upgraded upon the pipeline of Jarrett et al. 2012 and Jarrett et al. 2013) to perform photometric measurements on the WISE images. Here we briefly summarise the major steps of the procedure. For each image, the pipeline first removes nearby sources and produces a clean image. Then it obtains the aperture flux and SB radial profile within the 1σ (sky rms) isophote around the galaxy centre. A double Sérsic model is fitted to the SB profile, and the final total flux is calculated as the sum of the aperture flux and the extrapolation of the Sérsic model beyond the 1σ isophote out to three times the scale-length of the disc (the second component of the double Sérsic model). Calibration and spectral shape related corrections are applied to the magnitudes as described in Jarrett et al. (2016). Structural parameters like position angle and axis ratio b/a (minor-to-major axis ratio) of the outmost isophote, effective radius r_e (radius that enclose half of the total flux), effective surface brightness (the averaged surface brightness within r_e), and concentra-

tion indices R_{75}/R_{25} (the ratio between radii that enclose 75% and 25% of the total fluxes) are also derived.

Figure 5 shows the intermediate products of this pipeline for two galaxies, NGC 300 and ESO 381-G020. We are able to reliably measure total fluxes (with errors less than 0.5 mag) for 81, 76, 65 and 57 galaxies in the W1–4 bands. We are unable to measure W1 fluxes for only one galaxy, J1131-31, because a foreground star outshines the whole galaxy. We further impose the W1 aperture on the W2 image for the five galaxies detected in W1 but not in W2, and obtain a rough measure of the W2 flux by summing all pixels within the aperture.

As described in Jarrett et al. (2016), we obtain the rest-frame W1-4 fluxes based on these photometric fluxes. Especially, we remove the stellar continuum to obtain the W3 fluxes of the $11.3 \mu\text{m}$ PAH (polycyclic aromatic hydrocarbon) and the W4 fluxes originated from warm and cold small dust grains. These rest-frame and stellar continuum removed fluxes are obtained through comparing the WISE spectral energy distribution (SED) of each galaxy with extragalactic population SED templates built in Brown et al. (2014) based on the SWIRE/GRASIL models (Polletta et al. 2006, 2007; Silva et al. 1998). These corrected fluxes are more directly linked to physical quantities (e.g. M_* and SFR) than the photometric fluxes.

We present these WISE rest frame luminosities and structural parameters in Table A2.

3.3 Estimate of M_* and SFR

3.3.1 Estimating M_*

Using the method of Jarrett et al. (2012), we calculate the W1 band stellar mass-to-light ratio based on the W1-W2 colour to account for the stellar population dependence. Similar to the treatment in Jarrett et al. (2016), we put a floor/ceiling limits on the W1-W2 colour, -0.05 to 0.2 mag, the colour range where the Jarrett et al. (2012) formula was calibrated. It also minimises AGN contamination and the systematics caused by the less sensitive W2 band. Then we calculate M_* for 81 LVHIS galaxies based on W1 luminosities.

The Jarrett et al. (2012) method was calibrated using nearby bright spiral galaxies, so there might be a worry that it fails for low-mass irregular galaxies. Hence we compare our WISE-based M_* with the M_* derived from optical and H -band data in Figure 6. The CGS M_* is estimated with the $B - R$ colour dependent R -band mass-to-light ratios based on the formula in Bell et al. (2003). The H -band based M_* is taken from Kirby et al. (2012) and Young et al. (2014) and was estimated with a fixed mass-to-light ratio of 0.9. Finally, the SINGG M_* is estimated with a R -band luminosity dependent R -band mass-to-light ratio as discussed in Wong et al. (2016). The median and scatter of the differences in M_* are -0.04 and 0.23 dex respectively for the comparison between WISE and CGS (19 galaxies), -0.12 and 0.20 dex respectively for the comparison between WISE and H -band (22 galaxies), and 0.06 and 0.17 dex for the comparison between WISE and SINGG (13 galaxies). The scatter is consistent with the typical errors of M_* -to-light ratios with and without accounting for dependence on stellar populations (Bell et al. 2003). As can be seen from Figure 6,

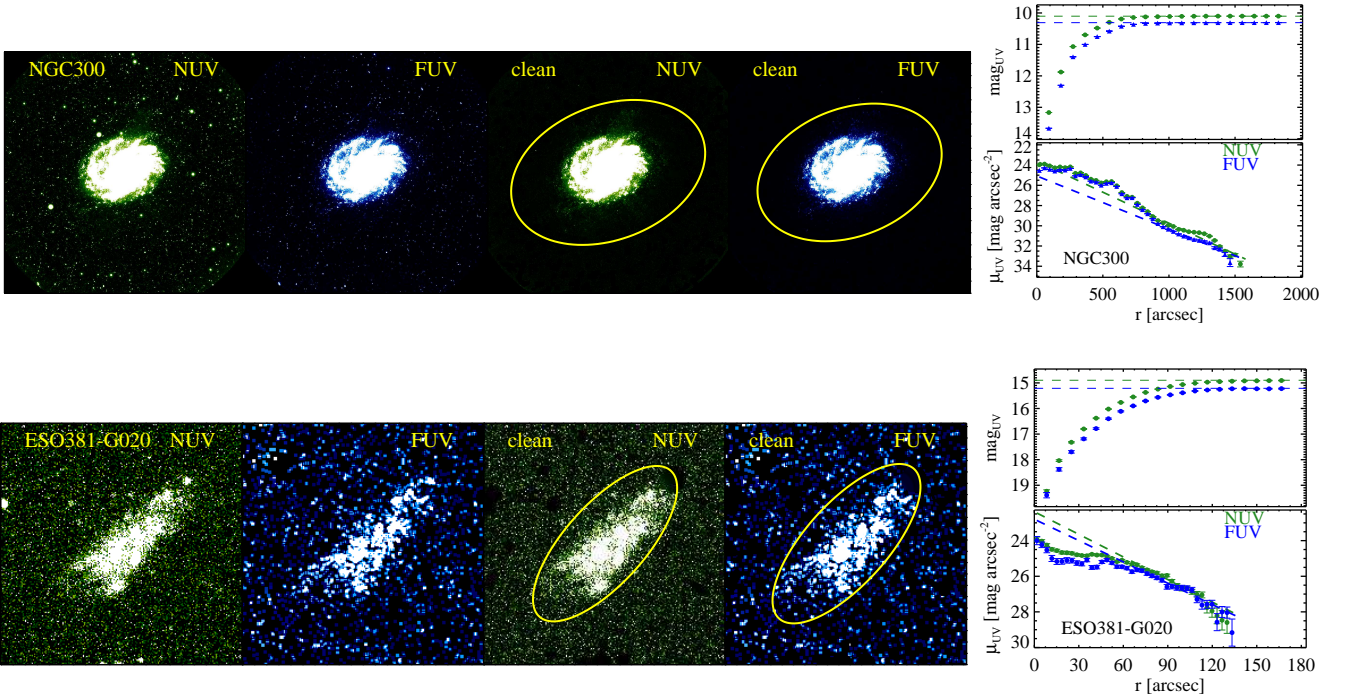


Figure 2. This gallery shows examples of the intermediate products of the GALEX photometry pipeline. The top row shows NGC 300, a UV-bright galaxy with DIS images, and the bottom row shows ESO 381-G020, a relatively UV-faint galaxy with only AIS images. The left four columns as denoted in the corner of each panel display the original FUV and NUV images, and clean images with contamination sources removed. The yellow ellipses show the isophotes for the last data points in NUV radial SB profiles. The right-most panels show the GCs (top) and the SB profiles (bottom).

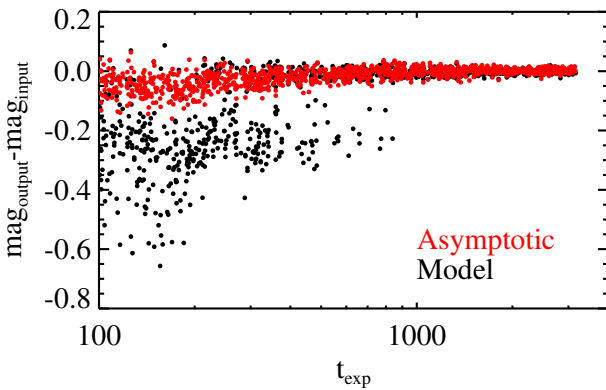


Figure 3. Stability of flux measurements at different image depths. Shallow images are simulated based on the deep GALEX FUV image of NGC 300 (see Section 3.1). Asymptotic and model magnitudes measured from shallow simulated images (output) are compared to the magnitude measured from the original deep image (input).

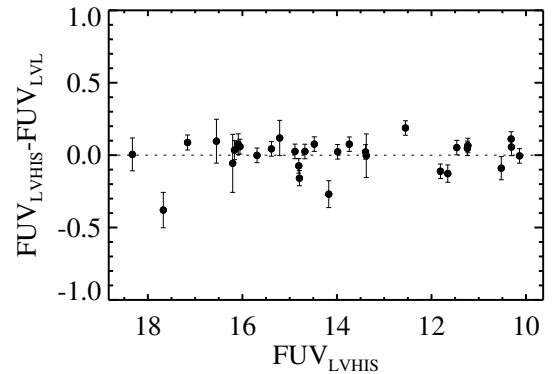


Figure 4. Comparison of GALEX FUV flux measurements between the LVHIS and LVL samples. The dashed line mark zero.

3.3.2 Estimating SFR

We estimate the dust un-attenuated part of the total SFR based on FUV luminosities (SFR_{FUV}), and recover the dust attenuated part based on W4 luminosities (SFR_{W4}). This method is widely adopted in the literature (Calzetti 2013; Hao et al. 2011) and based on the fact that FUV fluxes are primarily contributed by the massive B stars which have a typical age of 100 Myr, and part of the FUV fluxes are absorbed and re-emitted by cool and warm dust in the far and mid-infrared, while W4-band traces the warm dust with a temperature ~ 150 K.

CGS contains the massive LVHIS galaxies, the H -band survey focusses on dwarf galaxies, while SINGG connects the two populations. The WISE-based M_* estimates in this paper are in excellent agreement with the M_* estimates from optical and near-infrared luminosities for both dwarf and massive galaxies.

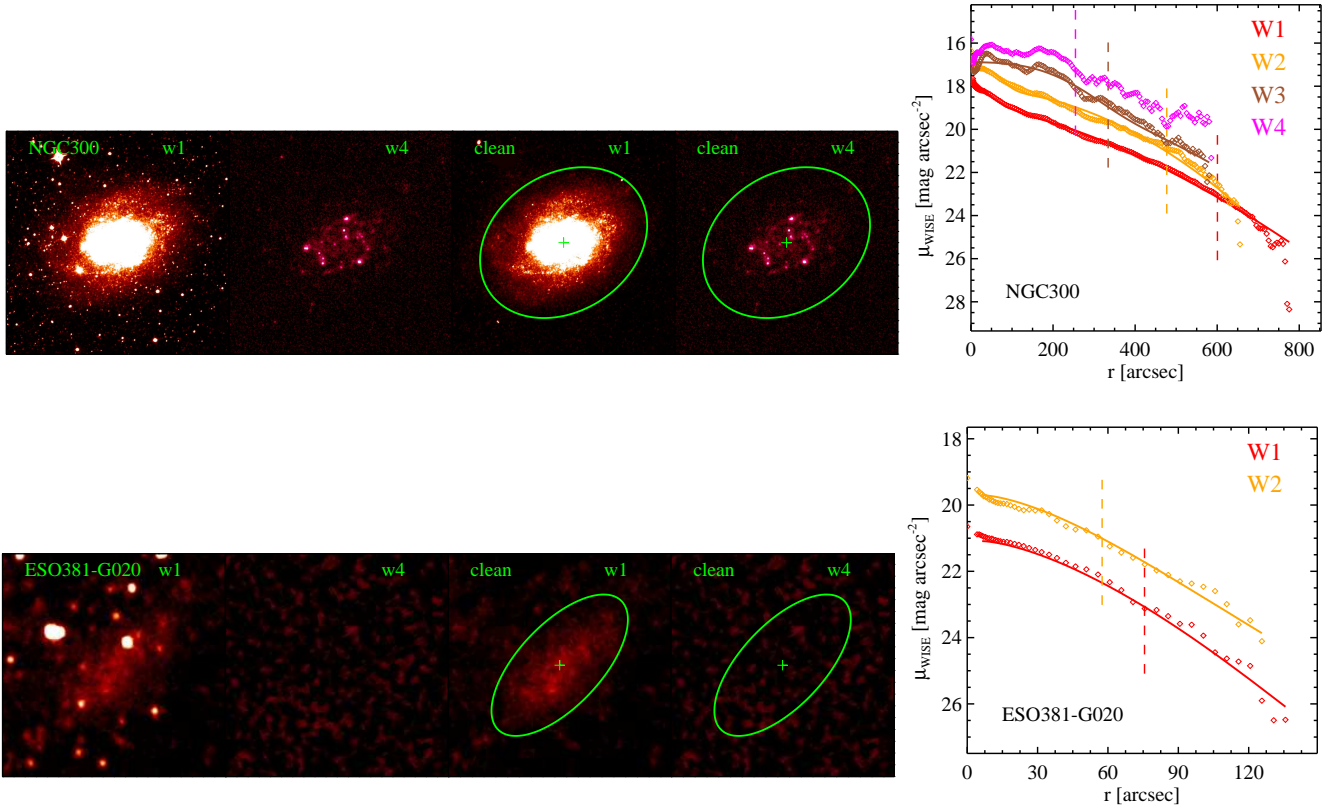


Figure 5. This gallery shows examples of the intermediate products of the photometry pipeline applied to the WISE images. The top row shows the bright spiral galaxy NGC 300, and the bottom row shows the much fainter dwarf irregular galaxy ESO 381-G020. From left to right, as denoted in the corner of each panel, we show the original W1 and W4 images, and the respective clean images, where foreground and background sources are removed. The right-most panels show the SB profiles and the Sérsic fits for both galaxies. The dashed vertical lines show where the SB profile reaches the sky rms.

We calculate SFR_{FUV} with the equation from Calzetti (2013, their table 1.2), which is derived from stellar population models (dust-free). We calculate SFR_{W4} with equation 2 from Jarrett et al. (2013), which is derived from the infrared SED models of starburst galaxies (SFR fully attenuated). Then total $\text{SFR} = \text{SFR}_{\text{FUV}} + \text{SFR}_{\text{W4}}$. Because FUV data are not always available while W4 fluxes are not always detectable for all the galaxies, we use the W4 estimated SFR as a lower limit when only W4 data is available, and assume the dust attenuation to be zero when we get no detection from the W4 data.

We also caution that while we have tried our best to remove the contribution from stellar continuum (Section 3.2), W4 band as an SFR indicator has uncertainties for being a far extrapolation of the dominant bolometric emission that arises from cool dust in the far-infrared, and it has risks of being contaminated by the warm and dusty TP-AGB populations. Hence for validation we compare in Figure 7 our SFR with SFR derived in other ways (see Section 2.4). The 11HUGS (FUV+TIR) SFR (from Lee et al. 2009) was estimated in a similar way as in this paper, but the more accurate attenuation tracer, total infrared luminosities (TIR) instead of $22 \mu\text{m}$ were used to indicate the dust attenuated SFR. The 11HUGS ($\text{H}\alpha$) SFR (also from Lee et al. 2009) was derived with the $\text{H}\alpha$ luminosities with a dust attenuation correction based on the Balmer decrement $\text{H}\alpha/\text{H}\beta$. The SINGG ($\text{H}\alpha$) SFR is estimated from the $\text{H}\alpha$ luminosities

with a dust attenuation correction determined by the R-band absolute magnitude (Meurer et al. 2006).

The LVHIS SFRs agree well with these three datasets, with a median difference of -0.08 ± 0.09 , 0.07 ± 0.36 and -0.02 ± 0.17 dex from the 11HUGS (FUV+TIR), 11HUGS ($\text{H}\alpha$) and SINGG ($\text{H}\alpha$) SFRs. When $\text{SFR} < 0.01 M_{\odot} \text{ yr}^{-1}$, 11HUGS ($\text{H}\alpha$) SFRs tend to be systematically lower than our SFRs, which might be caused by insufficient samplings of the massive end of the initial mass function (IMF), or by a different IMF shape at the massive end in the low gas surface density regions (Meurer et al. 2006; Lee et al. 2009; López-Sánchez et al. 2015). On the other hand, there is no systematic offset between LVHIS and SINGG ($\text{H}\alpha$) SFRs at the low SFR end.

4 ANALYSIS FOR THE LARGE LVHIS GALAXIES

4.1 Resolution-matched multi-wavelength photometry

We have selected ten well-resolved LVHIS galaxies for an analysis of radial distributions of multi-wavelength light. We use the pipeline of Wang et al. (2010) to perform resolution-matched photometric measurements from the GALEX, WISE and HI images. Instead of using the original GALEX and WISE images, we use the cleaned images (see

Table 1. Derived galaxy properties (to be continued).

ID	HIPASS ID	Galaxy Name	SFR	$\log M_*$	$\log f_{\text{HI}}$	R_{HI}/R_{25}^r	$\log \Sigma_{*,\text{eff}}$	$\log \Sigma_{\text{SFR},r<R_{25}}$	$\Sigma_{\text{HI},r<R_{25}}^r$	$\Sigma_{\text{HI},r<3.2r_s}^r$
(1)	(2)	(3)	$[M_{\odot} \text{ yr}^{-1}]$	$[M_{\odot}]$	(6)	(7)	$[M_{\odot} \text{ pc}^{-2}]$	$[M_{\odot} \text{ yr}^{-1} \text{ kpc}^{-2}]$	$[M_{\odot} \text{ pc}^{-2}]$	$[M_{\odot} \text{ pc}^{-2}]$
(4)	(5)	(8)	(9)	(10)	(11)					
1	J0008-34	ESO349-G031	0.0006±0.0001	7.3	-0.22	-	6.81	-2.92	-	0.35
2	J0026-41	ESO294-G010	0.0001±0.0001	6.7	-	-	7.36	-3.16	-	-
3	J0015-32	ESO410-G005	0.0001±0.0000	6.2	-0.32	-	6.72	-3.67	-	0.35
4 ^l	J0015-39	NGC55	0.1896±0.0220	9.4	-0.03	1.26	8.01	-3.14	6.53	3.39
5 ^l	J0054-37	NGC300	0.1598±0.0210	9.5	-0.21	2.30	7.91	-2.86	5.44	4.67
6 ^l	J0047-25	NGC253	3.8612±0.5582	10.4	-0.99	0.82	8.84	-2.38	2.94	7.13
7	J0047-20	NGC247	0.1374±0.0206	9.7	-0.42	1.33	7.92	-3.37	4.74	1.70
8	J0135-41	NGC625	0.0455±0.0051	8.7	-0.75	0.77	8.00	-2.97	1.83	2.29
9	J0145-43	ESO245-G005	0.0249±0.0037	8.3	0.27	2.60	7.15	-2.74	7.73	2.65
10	J0150-44	ESO245-G007	0.0000±0.0000	6.8	-1.85	-	6.73	-3.45	-	0.03
11 ^l	J0237-61	ESO115-G021	0.0133±0.0020	8.1	0.76	2.25	7.28	-3.48	5.09	3.72
12	J0256-54	ESO154-G023	0.0366±0.0055	8.7	0.27	-	7.32	-	-	-
13	J0258-49	ESO199-G007	0.0015±0.0004	7.0 ^h	0.23	-	-	-3.02	-	0.62
14 ^l	J0317-66	NGC1313	0.5164±0.0642	9.5	-0.20	1.65	7.83	-2.40	8.45	8.31
15	J0320-52	NGC1311	0.0128±0.0019	8.2	-0.29	1.18	7.69	-3.15	3.80	2.22
16	J0321-66	AM0319-662	0.0001±0.0001	7.1	-1.14	-	-	-4.35	-	-
17	J0333-50	IC1959	0.0261±0.0036	8.5	-0.19	1.55	8.02	-3.00	5.08	4.37
18	J0454-53	NGC1705	0.0481±0.0069	8.2	-0.37	-	8.15	-2.06	-	2.33
19	J0457-42	ESO252-IG001	-	7.3	0.76	2.11	6.77	-	-	2.95
20	J0605-33	ESO364-GQ029	-	7.6	0.90	2.14	6.46	-	-	2.57
21	J0607-34	AM0605-341	-	7.9	0.18	-	7.80	-	-	-
22	J0610-34	NGC2188	>0.0211±0.0036	8.9	-0.28	0.91	7.92	>-3.71	3.91	1.66
23	J0615-57	ESO121-G020	0.0033±0.0006	7.2	0.58	2.92	6.96	-2.66	-	1.38
24	J0639-40	ESO308-G022	-	7.8	-0.04	4.54	7.01	-	-	-
25	J0705-58	AM0704-582	-	6.2	2.09	-	6.76	-	-	-
26	J0731-68	ESO059-G001	-	8.1	-0.16	2.49	7.25	-	4.41	1.03
27	J0926-76	NGC2915	0.0265±0.0038	8.4	0.10	4.26	8.22	-2.32	4.64	2.27
28	J1043-37	ESO376-G016	-	8.0	0.07	4.00	7.26	-	-	-
29	J1047-38	ESO318-G013	0.0057±0.0017	7.4	0.60	-	6.85	-3.35	-	0.62
30	J1057-48	ESO215-GQ009	0.0442±0.0067	8.0	0.89	17.38	6.92	-1.19	-	4.92
31 ^l	J1118-32	NGC3621	0.7127±0.0775	9.7	0.28	3.44	8.28	-2.60	4.15	3.18
32	J1131-31	new	-	-	-	-	-	-	-	-
33	J1132-32	new	-	7.7	-0.70	-	7.04	-	-	-
34	J1137-39	ESO320-G014	-	8.1	-0.84	-	7.26	-	-	0.47
35	J1154-33	ESO379-G007	-	7.3	0.18	-	-	-	-	-
36	J1204-35	ESO379-G024	-	7.5	-0.37	-	7.28	-	-	-
37	J1214-38	ESO321-G014	0.0010±0.0001	7.0	0.06	1.79	7.06	-3.12	-	0.97
38	J1219-79	IC3104	-	8.2	-1.19	1.18	7.71	-	4.08	0.37
39	J1244-35	ESO381-G018	-	7.2	0.04	-	7.31	-	-	1.51
40	J1246-33	ESO381-G020	0.0097±0.0015	7.4	0.95	2.37	6.67	-3.06	-	2.33
41	J1247-77	new	-	7.1	-0.07	-	6.94	-	-	1.39
42	J1305-40	CEN06	0.0016±0.0005	7.8	-0.20	-	6.91	-3.57	-	0.53
43	J1305-49	NGC4945	>0.9566±0.1455	10.1	-1.01	0.90	8.58	>-2.74	2.56	5.39
44	J1310-46	ESO269-G058	0.0018±0.0004	8.5	-1.21	0.66	7.78	-3.81	1.60	0.62
45	J1321-31	new	0.0005±0.0001	-	-	-	-	-3.97	-	-

^h: *H*-band photometry based.

^l: Mark the sub-sample of large galaxies for detailed analysis (see Section 2.1 and 4).

Table 1. Derived galaxy properties (continued).

ID	HIPASS ID	Galaxy Name	SFR	$\log M_*^e$	$\log f_{\text{HI}}$	R_{HI}/R_{25}	$\log \Sigma_{*,\text{eff}}$	$\log \Sigma_{\text{SFR},r<R_{25}}$	$\Sigma_{\text{HI},r<R_{25}}$	$\Sigma_{\text{HI},r<3.2r_s}$
(1)	(2)	(3)	$[M_\odot \text{ yr}^{-1}]$	$[M_\odot]$	(6)	(7)	$[M_\odot \text{ pc}^{-2}]$	$[M_\odot \text{ yr}^{-1} \text{ kpc}^{-2}]$	$[M_\odot \text{ pc}^{-2}]$	$[M_\odot \text{ pc}^{-2}]$
(4)	(5)	(6)	(7)	(8)	(9)	(10)	(11)	(12)	(13)	(14)
46	J1321-36	NGC5102	-	9.5	-1.11	1.14	8.68	-	1.77	1.39
47	J1324-30	AM1321-304	0.0004±0.0006	7.9	-0.95	-	7.15	-3.99	-	0.65
48	J1324-42	NGC5128	0.7782±0.1038	11.0	-	-	9.00	-3.05	-	-
49	J1326-30	IC4247	0.0037±0.0006	7.5	-0.21	-	7.42	-2.97	-	1.12
50	J1327-41	ESO324-G024	0.0118±0.0019	8.0	0.20	2.36	7.23	-2.85	6.97	3.69
51	J1334-45	ESO270-G017	>0.0053±0.0012	8.7	0.10	1.36	7.41	>-4.33	4.02	3.34
52	J1336-29	UGCA365	0.0010±0.0003	7.2	0.25	-	7.01	-3.39	-	-
53 ^l	J1337-29	NGC5236	2.9211±0.3408	10.5	-0.59	2.62	8.50	-2.11	4.25	3.92
54	J1337-39	new	0.0012±0.0018	-	-	-	-	-3.55	-	-
55	J1337-42	NGC5237	0.0031±0.0007	8.3	-0.81	0.89	8.11	-3.07	1.99	1.03
56	J1337-28	ESO444-G084	0.0031±0.0005	6.9	1.00	2.89	6.75	-2.89	-	3.12
57	J1339-31	NGC5253	0.3606±0.0471	8.6	-0.66	0.95	8.38	-1.79	3.74	10.06
58	J1340-28	IC4316	0.0026±0.0004	7.9	-0.83	-	7.38	-2.26	-	0.33
59	J1341-29	NGC5264	0.0099±0.0015	8.7	-0.96	1.01	7.71	-3.20	2.65	0.43
60	J1345-41	ESO325-GQ011	-	7.1	0.72	1.79	6.71	-	6.77	2.79
61	J1348-37	new	-	-	-	-	-	-	-	0.29
62	J1348-53	ESO174-GQ001	-	7.6	0.57	-	7.65	-	-	2.36
63	J1349-36	ESO383-G087	>0.0022±0.0005	8.9	-1.09	0.92	7.85	>-4.07	2.47	0.63
64	J1351-47	new	-	-	-	-	-	-	-	-
65	J1403-41	NGC5408	>0.0197±0.0031	8.2	0.19	2.70	7.73	>-2.79	-	3.88
66	J1413-65	Circinus	>3.0452±0.4645	10.1	-0.26	5.63	-	>-1.46	3.72	3.88
67	J1428-46	UKS1424-460	-	7.5	0.18	-	7.04	-	-	3.71
68	J1434-49	ESO222-G010	-	7.8 ^h	-0.09	-	-	-	-	0.96
69	J1441-62	new	-	7.8	-0.47	-	8.16	-	-	-
70	J1443-44	ESO272-G025	-	8.0	-0.93	-	7.72	-	-	-
71	J1501-48	ESO223-G009	-	8.9	0.13	-	7.67	-	-	5.32
72	J1514-46	ESO274-G001	>0.0101±0.0016	9.0	-0.52	1.26	7.96	>-3.78	3.67	3.94
73	J1526-51	new	-	6.9	0.66	-	-	-	-	-
74	J1620-60	ESO137-G018	-	8.4	0.19	1.36	7.55	-	8.19	0.84
75	J1747-64	IC4662	0.0485±0.0058	8.0	0.15	4.68	7.92	-1.59	-	8.48
76	J2003-31	ESO461-G036	-	8.1	-0.12	5.12	7.09	-	-	1.73
77 ^l	J2052-69	IC5052	0.0613±0.0068	9.1	-0.20	1.33	8.02	-3.30	3.92	2.42
78 ^l	J2202-51	IC5152	0.0161±0.0022	8.2	-0.20	1.85	7.88	-2.59	8.03	4.73
79	J2326-32	UGCA438	0.0013±0.0002	6.9	-0.25	-	6.86	-2.83	-	0.37
80	J2343-31	UGCA442	0.0080±0.0012	7.3	1.01	1.81	6.95	-3.33	7.02	3.47
81	J2352-52	ESO149-G003	0.0073±0.0011	7.4	0.36	-	7.52	-3.14	2.12	-
82 ^l	J2357-32	NGC7793	0.2526±0.0307	9.5	-0.53	1.30	8.03	-2.64	6.22	4.22

Section 3.1 and 3.2). We remove the background and set all pixels beyond the ellipse defined by the last measured point in the SB profile to zero. By doing so, we minimise possible contamination from nearby sources in the following step of resolution matching.

Because the PSFs of WISE images are known to have significant side-lobes, we convolve the WISE cleaned images with the kernels from Aniano et al. (2011), which convert the WISE PSFs to PSF shapes described by Gaussian functions. After this convolution process, the W1, 2 and 4 images have Gaussian-shaped PSFs with FWHM of 7.5, 8.0 and 15.0 arcsec, respectively.

For each galaxy the HI image, which has the lowest resolution, is used as the reference image. All other images are registered and convolved to have the same geometry

and PSF resolution as the reference image. The resolution matched images for the whole sub-sample have a physical spatial resolution between 0.3 to 2.5 kpc, and a median value of 1.5 kpc. We show the stellar mass and SFR images derived based on these images, as well as the relation matched HI images in Figure B1.

We measure radial SB profiles from these images. SB is azimuthally averaged in elliptical rings with a position angle and axis ratio determined from the WISE W1 images (Section 3.2). We apply a projection correction to SB by multiplying them with the axis ratio b/a (assuming very thin discs). The major axis of each ring is taken as the profile radius. We limit the outermost radius of each profile to be the same as the profile measured from the original image before convolution, because we have removed all pixels outside

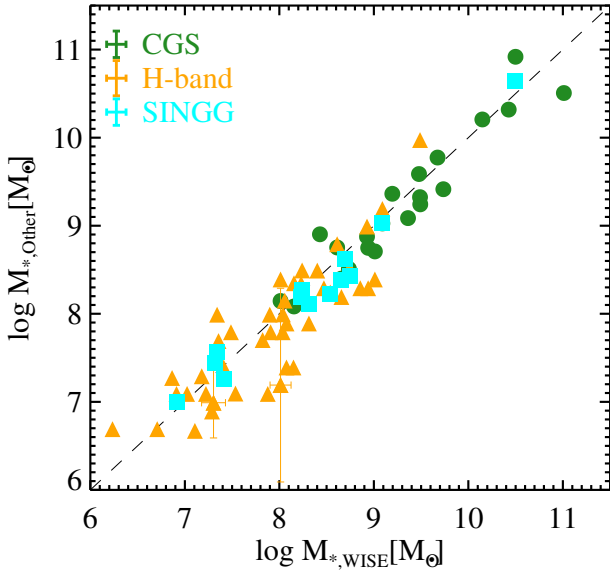


Figure 6. Comparison of WISE-based M_* (this work) with the estimates from other published data (see Section 3.3.1). The dashed line marks the one-to-one relation. Typical error bars are shown in the left-top corner. Measurements from different datasets have been adjusted to have the same luminosity distance and Kroupa (2001) IMF before comparison.

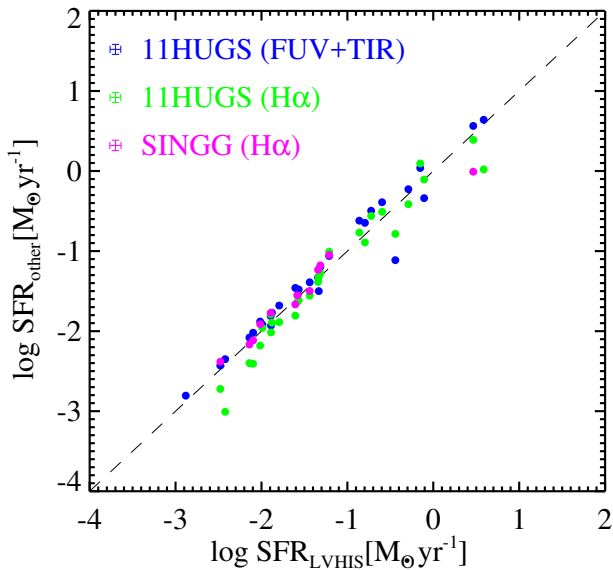


Figure 7. Comparison of FUV+W4 based SFR (this work) with the estimates from other published data (see Section 3.3.2). The dashed line marks the one-to-one relation. Typical error bars are shown in the left-top corner. Measurements from different datasets have been adjusted to have the same luminosity distance and Kroupa (2001) IMF before comparison.

that radius before the image resolution matching step. We use the background noise from the original images to estimate photometric errors, as the noise has become correlated in the resolution-matched images.

Finally, M_* and SFR profiles are calculated based on these SB profiles. When deriving M_* , we use the W1 SB profile and a fixed mass-to-light ratio determined by the total

W1–W2 colour, because the W2 SB profiles do not extend as far as the W1 SB profiles in most of the galaxies while our study focuses on the outskirts of galaxies. When deriving SFR profiles, the W4 SB profiles also end at much smaller radius than the FUV SB profiles, so we exponentially extrapolating the SFR_{W4} profiles in order to obtain total SFR profiles. In most galaxies, the extrapolated SFR_{W4} profile in the outer region is lower than the SFR_{FUV} profile, which alleviates the uncertainties caused by extrapolation.

We obtained the surface densities (Σ) at the radius where $\Sigma_{\text{HI}} = 3 M_{\odot} \text{pc}^{-2}$, where $\Sigma_* = 3 M_{\odot} \text{pc}^{-2}$ and at $r = 1.25 R_{25}$. This allows us to study the $\Sigma_{\text{SFR}}-\Sigma_{\text{HI}}$ relation when fixing Σ_* at $3 M_{\odot} \text{pc}^{-2}$, the $\Sigma_{\text{SFR}}-\Sigma_*$ relation when fixing Σ_{HI} at $3 M_{\odot} \text{pc}^{-2}$, and both relations at $1.25 R_{25}$ ¹. These investigations will be presented in Section 7. When the radial positions are outside the radial range of a profile (in all cases, Σ_* profiles), we obtain the surface densities through linearly extrapolating in logarithmic space the exponential outer part of the radial profiles. Most of the extrapolated radii are within 1.2 times the last data point of the profiles. The error of an extrapolated surface density is a combination of the extrapolated measurement error and the f-test based model error.

These resolution-matched M_{HI} , M_* and SFR radial profiles and measurements are presented in the last column of Figure B1.

Regarding extrapolating the Σ_* profiles, one may worry about the fact that optical and mid-infrared radial profiles frequently bend up or downward in the galactic outskirts (Pohlen & Trujillo 2006). However, there is evidence that Σ_* radial profiles are much less bent than the surface brightness profiles (Bakos et al. 2008), and we are not extrapolating far away from the last measurable data points. These two facts to some extent alleviate the problem of bending profiles. Nevertheless, optical or MIR images that are deep, of high-resolution (to suppress confusion noise), and of large field-of-view (to homogeneously cover the outskirts of the galaxies) are needed for a future confirmation of our results. Such kind of data will be available with the completion of wide-field optical imaging surveys, like the Skymapper Southern Sky Survey (Keller et al. 2007).

4.2 HI tilted ring models

4.2.1 Building the HI tilted ring models

We make use of Fully Automated TiRiFiC (Kamphuis et al. 2015, FAT), which builds on the 3D Tilted Ring Fitting Code (TiRiFiC Józsa et al. 2007, J07 hereafter), to derive tilted ring models and rotation curves for the large LVHIS galaxies. The approaching and receding velocity sides are modelled separately. Part of the sample has already been processed by Kamphuis et al. (2015) using FAT, including NGC 253, NGC 1313 and IC 5152. We present the model rotation curves and radial profiles of position angles, inclinations and surface densities in Figure B2 in the appendix.

In Figure B2, we can see that at the optical radius

¹ We caution that there is faint Galactic cirrus in the foreground of NGC 1313 which may affect the Σ_{SFR} measurements in the outskirts (Contursi et al. 2002). On the other hand, removing NGC 1313 from our sample does not change our conclusion.

R_{25} , the HI and optical inclinations usually agree within 20° . At R_{25} , PA (position angle) from the two bands also agree within 20° for most of the galaxies, except for NGC 5236 (PA from the two bands differ by $\sim 60^\circ$). Tilted ring models mostly provide a fit considering kinematics, while in the optical they are not taken into account. Below an inclination of 40° it becomes very difficult to accurately measure PAs without kinematical information, which might explain the discrepancy between the optical and kinematical PAs for NGC 5236.

If we assume the extent of fluctuations to reflect fitting uncertainties, the 3D de-projected radial HI profiles (as an output of FAT) generally agree well with the radial HI profiles which are measured and corrected for projection effects from the 2D moment-0 images (see Section 2.1 and Wang et al. (2016)).

We use the model results on both the approaching and receding velocity sides of galaxies to analyse HI warp related properties (see next section), and use the average of the two sides to study the relation between SFR and mass radial surface densities (Section 4.2.3 and 7).

4.2.2 Tiltograms and identification of warps

As summarised in the introduction of Józsa (2007), an HI warp is the inner plane of an HI disc kinematically bending in the outer region, and very often transiting into another plane. Józsa (2007) demonstrated that the “tiltograms” are very useful for identifying HI warps.

As outlined in Józsa (2007), a tiltogram is a pixel map showing the mutual inclination angle (θ_{tilt}) between rings at different radius. The pixel value (θ_{tilt}) at $x=r1$ and $y=r2$ in the map measures the angle between the normal vectors of the tilted rings at radius $r1$ and $r2$. The direction of the normal vector for each tilted ring is fully described by the position angle and inclination angle of the tilted ring. A completely flattened disc plane has a tiltogram with zero value in all pixels.

A tiltogram can be divided into four regions at a radius r , where the bottom-left square region with $x < r$ and $y < r$ shows the intrinsic mutual inclination of the disc within r (θ_{tilt}^{in}), the top-right square region with $x > r$ and $y > r$ shows the intrinsic mutual inclination of the disc outside r (θ_{tilt}^{out}), and the remaining two rectangles (which are identical to each other) showing the mutual inclination between the discs within and beyond r (θ_{tilt}^{mut}).

If a galaxy has an HI warp starting from radius r_{warp} , r_{warp} will divide the tiltogram into four regions as described above, where θ_{tilt}^{in} are close to zero and nearly constant, while θ_{tilt}^{mut} are large. When an outer disc plane exists beyond r_{warp} , θ_{tilt}^{out} are also close to zero and nearly constant. So we calculate the average θ_{tilt} ($\overline{\theta_{tilt}}$) in the four regions divided by each radius r , and set the criteria that an HI disc is classified as warped if a radius r_{warp} can be found where

- (i) $|\overline{\theta_{tilt}^{in}} - \overline{\theta_{tilt}^{mut}}|$ is a local maximum,
- (ii) $\overline{\theta_{tilt}^{in}} < 5$ deg, and
- (iii) $\overline{\theta_{tilt}^{mut}} > 10$ deg.

$\overline{\theta_{tilt}^{in}}$ indicates the flatness of the inner disc, $\overline{\theta_{tilt}^{mut}}$ indicates the warp angle, and $\overline{\theta_{tilt}^{out}}$ indicates the flatness of the outer disc.

We set the criteria in a relatively arbitrary way, which can be biased toward selecting the strongly warped HI discs. But it is sufficient for our scientific aim of investigating the influence of warps on SFE, as strong warps should have stronger effects than weak warps.

Because a galaxy can be warped on only one side of the galaxy, we analyse the approaching and receding side of the velocity field separately. We display the tiltograms for the approaching velocity side of the LVHIS large galaxies in the fifth column of Figure B2. The tiltogram of NGC 300 is a perfect example showing warp features, where r_{warp} is marked by purple lines. We notice from the tiltograms that sometimes one ring deviates abruptly from adjacent rings (e.g. at the radii $7.5'$ in IC5052). This kind of feature occurs when the tilted rings warping dramatically from one side to the other side of the inner plane.

We list the $\overline{\theta_{tilt}}$ and r_{warp} measurements in Table 2 for the approaching and receding velocity side respectively. We find HI warps on the approaching velocity side in seven out of the ten large LVHIS galaxies except for NGC 253, ESO115-G021 and NGC 1313 for which $\overline{\theta_{tilt}^{mut}}$ are too small. The same result is found on the receding velocity side.

4.2.3 Dark matter and stellar volume densities

In Section 7, motivated by the mid-plane pressure models for star formation (Ostriker et al. 2010; Krumholz 2013), we will study the dependence of SFR surface densities on the volume densities of stars and dark matter added together (σ_{sd}). In order to obtain a rough estimate of the parameter σ_{sd} , we make use of the tilted ring models derived in Section 2, which have been de-convolved with their PSF. So when we derive the Σ_* and Σ_{SFR} radial profiles, we perform a resolution matched photometry as in Section 4.1, but at the resolution of the W4 images.

We use the radial HI profiles from the tilted ring models. We use Equation 3 provided by Bigiel et al. (2008) to estimate the molecular hydrogen surface density Σ_{H_2} from Σ_{SFR} . The atomic and molecular hydrogen gas surface densities are multiplied by 1.36 to account for the helium gas. We use the sum of gas and stellar surface densities to approximate the baryonic mass densities. We use the rotation curves to estimate the total mass at each radius (M_{tot}). We subtracted from M_{tot} the contributions of stars and gas, and obtain the mass of the dark matter halo. We then assume a simple spherical model to calculate the volume density of the dark matter halo, σ_{dm} . These calculations are crude, while a more detailed decomposition of the different masses is beyond the scope of this paper.

Following the method in Leroy et al. (2008), we assume a fixed ratio of 7.3 between the scale-length and the scale-height (h) for the stellar discs, and calculate the volume density of stars as $\sigma_* = \Sigma_*/(4h) = \Sigma_*/(0.54r_s)$. Finally $\sigma_{sd} = \sigma_* + \sigma_{dm}$.

5 LVHIS GALAXIES AND THE HI RADIAL DISTRIBUTIONS

We have built a multi-wavelength dataset for the LVHIS sample, based on which we have derived M_{HI} , M_* and SFR.

Table 2. Measurements from the tiltograms of the ten large LVHIS galaxies.

Galaxy name	Approaching side					Receding side				
	$\overline{\theta_{tilt}^{in}}$ [deg]	$\overline{\theta_{tilt}^{out}}$ [deg]	$\overline{\theta_{tilt}^{mut}}$ [deg]	r_{warp}^1 [arcmin]	r_{warp}/R_{25} [deg]	$\overline{\theta_{tilt}^{in}}$ [deg]	$\overline{\theta_{tilt}^{out}}$ [deg]	$\overline{\theta_{tilt}^{mut}}$ [arcmin]	r_{warp}^1	r_{warp}/R_{25}
NGC 55	2.6	10.3	21.7	14.7	0.93	3.2	4.9	12.6	20.0	1.36
NGC 300	0.9	9.4	20.5	10.2	1.05	0.6	8.3	17.8	10.2	1.05
NGC 253*	0.0	1.1	2.3	4.2	0.28	0.0	1.0	2.1	4.2	0.28
ESO115-G021*	0.2	5.7	8.9	3.7	1.50	0.4	4.7	7.2	3.5	1.42
NGC 1313*	0.3	4.2	3.8	2.2	0.41	0.2	6.8	7.5	2.7	0.50
NGC 3621	1.4	5.5	15.4	12.4	2.56	3.6	5.5	21.0	14.7	3.02
NGC 5236	3.0	7.3	22.6	10.0	1.30	1.8	20.5	29.5	6.9	0.89
IC 5052	2.0	17.2	18.6	3.1	0.88	0.9	7.4	14.5	3.4	0.95
IC 5152	0.0	10.0	17.5	1.9	0.76	0.2	8.8	17.3	2.0	0.82
NGC 7793	3.1	5.1	17.5	6.3	1.22	1.6	3.6	11.1	6.2	1.19

¹: the radius identified based on the warp identification criteria 1.

*: galaxies that do not meet the warp identification criteria 2 and 3 in Section . As we have adopted relatively strict criteria that are biased toward strong warps, we provide warp related parameters for these un-warped galaxies to show the full parameter space of the sample.

In this section, we compare the distribution of these parameters with other surveys to understand the selection effect and the advantage of LVHIS. We also investigate how HI is radially distributed with respect to the optical discs and how it depends on the HI-richness of galaxies. By assessing the diversity of radial HI distributions, we better understand what new information is gained with interferometry data, and why they are useful for understanding global scaling relations in the next section.

5.1 LVHIS compared to other HI samples

This section compares the the f_{HI} and SFR distributions of the LVHIS sample with other HI samples.

In Figure 8, we can see that M_* of LVHIS ranges from $10^6 M_{\odot}$ to $10^{10.5} M_{\odot}$ and has a median $\sim 10^8 M_{\odot}$. The sample covers nearly two orders of magnitude in f_{HI} ($= M_{HI}/M_*$) at a fixed M_* . For example, at $M_* \sim 10^8 M_{\odot}$, f_{HI} ranges from -1.2 to 1 dex.

The left panel of Figure 8 compares LVHIS with several single-dish HI datasets. We can see that most of the LVHIS galaxies have lower M_* than the median M_* of ALFALFA, GASS and HRS. Their f_{HI} are typically lower the median f_{HI} of ALFALFA at a fixed M_* , and comparable to an extrapolation of the $f_{HI}-M_*$ distribution to the lower M_* side for GASS and HRS.

In the right panel of Figure 8, we compare LVHIS to several HI interferometry surveys. We can see that both LVHIS and WHISP tend to connect the existing resolved HI samples of irregular galaxies (like LITTLE THINGS and FIGGS) and massive spiral galaxies (like THINGS) in the $f_{HI}-M_*$ space. WHISP provides a wider M_* distribution than LVHIS, while LVHIS detects galaxies with on average lower f_{HI} at a fixed M_* than WHISP. On the other hand, the LVHIS large galaxies sample, in comparison to the rest LVHIS galaxies, are biased toward systems with high f_{HI} for their M_* .

These comparisons suggest LVHIS as (or close to) a volume-limited HI sample covers a wide range of both M_* and f_{HI} . It is not significantly biased to high f_{HI} galaxies compared to single dish samples, hence has the ability to

explore the cause for global scaling relations using spatially resolved HI distributions; it includes both spiral and irregular galaxies, hence has the ability to explore general physics at work in these two types of galaxies. This paper will make use of these advantages.

In Figure 9, we show that most of the LVHIS galaxies lie below the star-forming Main Sequence (MS) from SDSS (Renzini & Peng 2015) and also below the mean SFR- M_* relations for ALFALFA (Huang et al. 2012b), WISE-GAMA (Jarrett et al. 2016) and WISE-GALEX (Grootes et al. 2013). This is consistent with the result that most LVHIS galaxies lie below the mean $f_{HI}-M_*$ relation for ALFALFA, which is close to the MS of low redshift galaxies (Huang et al. 2012b). It confirms the previous finding that the SFR- M_* and $f_{HI}-M_*$ relations mimic one another (Saintonge et al. 2016; Brown et al. 2015). On the other hand, most of the LVHIS galaxies have $\log \text{sSFR} (= \log \text{SFR}/M_*) > -11.5$, indicating most of them to be star-forming galaxies.

5.2 Radial distribution of HI gas

This section investigates the diversity of HI radial distributions in the LVHIS galaxies.

In Figure 10, we find that galaxies with higher f_{HI} on average have larger HI discs with respect to the optical discs (R_{HI}/R_{25} , top panel), and lower fractions of total HI masses enclosed within the optical discs ($M_{HI,r < R_{25}}/M_{HI}$, middle panel), but higher average HI surface densities within the optical discs ($\Sigma_{HI,r < R_{25}}$, bottom panel). However, the three correlations have considerable scatter. For example, when $f_{HI} = 1$, R_{HI}/R_{25} ranges from 1.25 to 6.3, $M_{HI,r < R_{25}}/M_{HI}$ ranges from 0.1 to 0.7, and $\Sigma_{HI,r < R_{25}}$ ranges from 4 to 8 $M_{\odot} \text{ pc}^{-2}$, within the LVHIS sample.

So there are a large variety of HI radial distributions at a fixed global properties. Because the inner disc within R_{25} contains the bulk of star formation in galaxies, directly measuring the properties of HI gas within R_{25} is important for understanding the intrinsic physics underlying the star formation-HI global scaling relations.

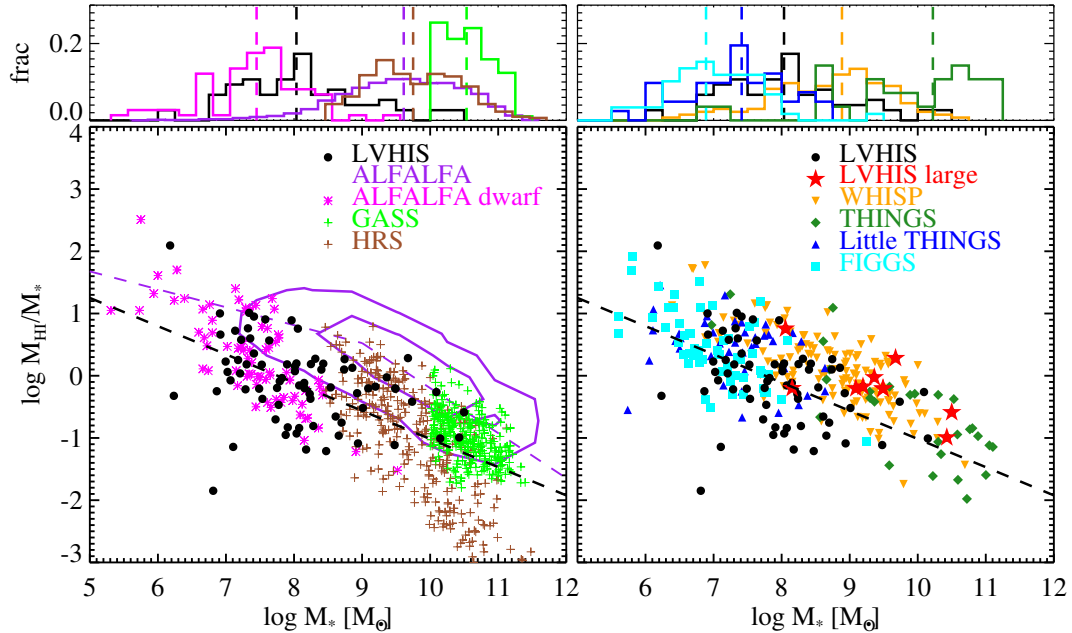


Figure 8. HI fraction ($f_{\text{HI}} = M_{\text{HI}}/M_*$) as a function of M_* for all LVHIS galaxies compared to other HI surveys obtained with single dish telescopes (left) and interferometers (right). The left panel compares LVHIS with surveys with single-dish HI data, including LVHIS, ALFALFA (Huang et al. 2012b), ALFALFA dwarf sample (Huang et al. 2012a), GASS (Catinella et al. 2013) and HRS (Boselli et al. 2014). M_* values are taken from the MPA/JHU catalog for the ALFALFA and GASS samples, from Huang et al. (2012a) for the ALFALFA dwarf sample, and from Cortese et al. (2012) for HRS. The right panel shows samples from HI interferometric surveys, including LVHIS, WHISP (Swaters et al. 2002), THINGS (Walter et al. 2008), Little THINGS (Hunter et al. 2012) and FIGGS (Begum et al. 2008). M_* are calculated from the B -band luminosities with mass-to-light ratios determined by the $B - V$ colour (formula from Bell et al. 2003) for the THINGS, Little THINGS and FIGGS samples. The THINGS B -band magnitudes are from SIMBAD astronomical database (Wenger et al. 2000), and V -band magnitudes are from Walter et al. (2008). The Little THINGS B - and V - magnitudes are from Hunter & Elmegreen (2006). The FIGGS B - and V - magnitudes are from Begum et al. (2008). The WHISP M_* are calculated from the B -band luminosities with mass-to-light ratio determined by the $B - R$ colour (formula from Bell et al. 2003). The WHISP B -band magnitudes are from Swaters et al. (2002), and R -band magnitudes are from Swaters & Balcells (2002). Different samples are shown in different colours and symbols as denoted in the right-top corner of each panel. The purple contours on the left panel show the distributions of 65% and 95% of the data points from the ALFALFA sample (Huang et al. 2012b). The dashed purple line in the bottom-left panel shows the mean relation for the ALFALFA sample (Huang et al. 2012b). The dashed black lines in the bottom panels show the linear fit to the $\log M_*$ - $\log f_{\text{HI}}$ relation for LVHIS. The dashed lines in the top panels show the median values of M_* distributions.

6 SFR-HI RELATIONS ON GALACTIC SCALES AND WITHIN R_{25}

In this section, we investigate on galactic scales the relation between SFR and HI mass and the dependence of SFE on other parameters. The reciprocal of SFE is also referred to as the HI depletion time, t_{dep} . Because both SFR and SFE are higher within the optical discs (within R_{25}) than beyond the optical discs (Bigiel et al. 2010), we also analyse SFR, M_{HI} and SFE measured within R_{25} .

6.1 The SFR- M_{HI} relation

In the left-top panel of Figure 11, we show tight scaling relations between SFR and M_{HI} and between SFR and $M_{\text{HI}, r < R_{25}}$ (left panels). This is consistent with the finding of ALFALFA (Huang et al. 2012b). On the other hand, Bigiel et al. (2008) found that Σ_{SFR} and Σ_{HI} are not correlated on kpc-scales within R_{25} . A question is whether there is an underlying intrinsic correlation between Σ_{SFR} and Σ_{HI} on galactic scales that differs from the relation on kpc-scales, because after all, HI is the reservoir of material for forming molecular gas and subsequently stars.

We investigate the correlations between Σ_{SFR} and Σ_{HI} averaged within R_{HI} and R_{25} (right panels), and find they are weak, in agreement with findings by Bigiel et al. (2008). Hence we conclude that on galactic scales and within R_{25} , SFR and M_{HI} are correlated mostly because both they both are correlated with the size of the galaxies, but not because of a physical link between star formation and HI gas.

We obtain a partial correlation coefficient of 0.84 for the relation between SFR and M_{HI} with the effect of M_* removed. So the SFR- M_{HI} relation is not caused by a correlation of both parameters with M_* .

6.2 Star Formation Efficiency

We investigate the dependence of SFE on other galactic properties, and compare the trends measured globally and within R_{25} . If the global trend reflects a mechanism that directly regulates the efficiency for HI to fuel star formation, then we should observe a correlation within R_{25} that is stronger than or similar to the one measured globally; but if the global trend is caused by the fact that the HI discs are much more extended than the stellar discs (so the gas cannot directly fuel the bulk of the star formation), then the trend

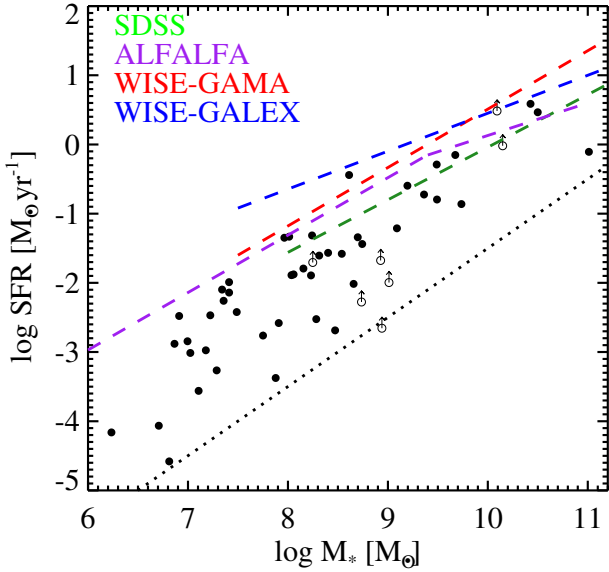


Figure 9. The distribution of LVHIS galaxies around the star-forming Main Sequence (MS). The open circles and upward arrows show the lower limits of SFR estimate. The green line is the MS from the SDSS sample (Renzini & Peng 2015), the purple, red and blue dashed lines are the mean relations from ALFALFA (Huang et al. 2012b), the WISE-GAMA sample (Jarrett et al. 2016) and the GALEX-GAMA sample (Grootes et al. 2013). The black dotted line shows the position for $\log \text{sSFR} (= \log \text{SFR}/M_*) = -11.5$.

should disappear when the relevant properties are measured within R_{25} .

In Figure 12, we can see that the SFE is significantly correlated with $\Sigma_{*,\text{eff}}$, moderately anti-correlated with f_{HI} , weakly anti-correlated with $M_{\text{HI},r<R_{25}}/M_{\text{HI}}$, hardly correlated with M_* , and not correlated with $\Sigma_{\text{HI},r<R_{\text{HI}}}$ or sSFR. In Figure 13, we can see that when we use $M_{\text{HI},r<R_{25}}$ instead of M_{HI} in these relations, $\text{SFE}_{r<R_{25}} (= \text{SFR}/M_{\text{HI},r<R_{25}})$ are still significantly correlated with $\Sigma_{*,\text{eff}}$ and moderately (weakly) anti-correlated with $f_{\text{HI},r<R_{25}} = M_{\text{HI},r<R_{25}}/M_*$, while the weak anti-correlation with $M_{\text{HI},r<R_{25}}/M_{\text{HI}}$ disappears. All other correlations remains weak considering the error bars. The direct implications seem to be that $\Sigma_{*,\text{eff}}$ and f_{HI} are related to mechanisms that directly regulate star formation fuelling in the stellar disc, while the HI radial distributions (indicated by $M_{\text{HI},r<R_{25}}/M_{\text{HI}}$) may only have a rather minor effect on the global SFE values.

Because f_{HI} and $\Sigma_{*,\text{eff}}$ are strongly correlated, we calculate the partial correlation coefficient between $\text{SFE}_{r<R_{25}}$ and $f_{\text{HI},r<R_{25}}$ with the dependence on $\Sigma_{*,\text{eff}}$ removed, and the value is -0.03 ± 0.23 . It suggests that SFE depends on $f_{\text{HI},r<R_{25}}$ only through their dependence on $\Sigma_{*,\text{eff}}$.

The correlation between SFE and $\Sigma_{*,\text{eff}}$ is consistent with the best-fit linear relation from Wong et al. (2016). The slope of the relation was explained in Wong et al. (2016) with a model where the galaxy discs are in a marginally stable status described by a constant two-fluid (gas and stars) Toomre Q parameter and the mid-plane pressure determines the molecular-to-atomic ratio. In such a model, a galaxy with high stellar surface density will have low gas surface density as adjusted by the constant Q ; the combined effects of high stellar surface density and low gas surface density

on the mid-plane pressure model result in very little change in the molecular gas mass (which SFR directly scales with); hence finally SFE as the ratio between SFR and HI surface densities increases.

To summarize, on galactic scales and within R_{25} , among the parameters investigated here SFE depends most strongly on the averaged stellar surface density $\Sigma_{*,\text{eff}}$.

7 STAR FORMATION BEYOND R_{25}

In this section we study the star formation on local scales in the outskirts of galaxies (beyond R_{25}), where both gas and stars are of low surface density and HI dominates the cold gas.

7.1 The dependence of Σ_{SFR} on Σ_* and Σ_{HI}

The investigation is based on the sub-sample of ten large galaxies (Section 2.1). First of all, we show in Figure 14 the relation between Σ_{HI} and Σ_{SFR} measured in pixels with sizes equivalent to the PSF FWHM beyond R_{25} . The distribution of data points and the mean relation are consistent with those from Bigiel et al. (2010).

As discussed in Section 1, in dwarf galaxies the radial variation of Σ_{SFR} follows the variation of Σ_* better than that of Σ_{HI} (Hunter et al. 1998). We ask whether we can observe the same phenomenon for the galactic outskirts of more massive galaxies. Because Σ_* , Σ_{HI} and Σ_{SFR} all generally decrease with increasing radius, we fix (control) Σ_{HI} when studying the dependence of Σ_{SFR} on Σ_* , and fix Σ_* when studying the dependence of Σ_{SFR} on Σ_{HI} . Limited by the data depth for Σ_* , we rely on the azimuthally averaged measurements in order to get enough signal-to-noise (S/N) ratio for Σ_* measurements in these low surface brightness galactic outer regions. Radial analysis may have the risk of smoothing out/integrating correlations, but is the best we can do for now. We note that very deep optical or MIR images (to trace stellar mass) will be needed in the future to confirm our results with a pixel-based analysis in a similar way as in Figure 14.

We analyse our data in two different ways, basing on resolution-matched radial profiles and profiles at the best resolution possible, respectively.

7.1.1 Analysis based on the resolution-matched radial measurements

We use the resolution-matched radial profiles derived in Section 4.1. The result is shown in Figure 15. The top-left panel shows the data points measured at $1.2R_{25}$ confirming the $\Sigma_{\text{SFR}}-\Sigma_{\text{HI}}$ relation from pixel-based analysis (Figure 14 and Bigiel et al. 2010). The data points suggest an HI depletion time longer than the Hubble time, but are systematically higher in Σ_{SFR} than the median relation from Bigiel et al. (2010). This difference comes from two effects. The first effect is the trend of SFE decreasing with galactocentric radius (the Bigiel et al. (2010) relation is a median relation for the radial region 1-2 R_{25}); the second effect is a difference between the mean and median relations noticed before in Roychowdhury et al. (2015). The best-fit relation from the data in this figure has a power law slope of 1.24 ± 0.36 . The

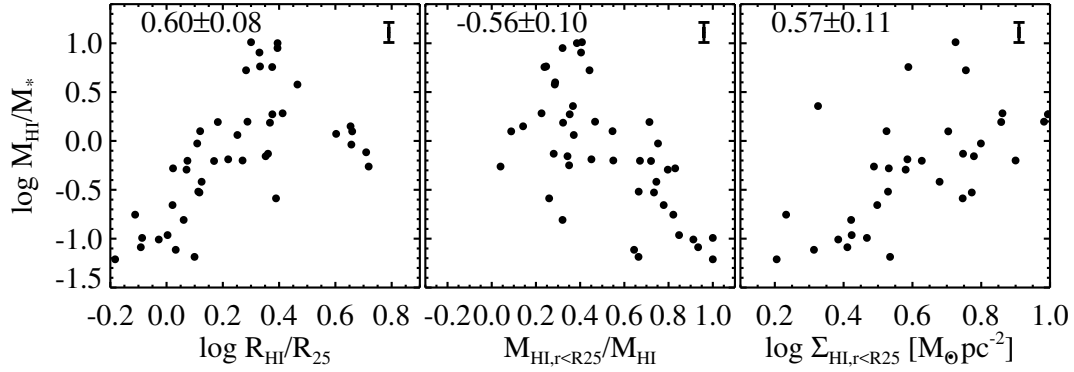


Figure 10. Distribution of HI gas with respect to the optical disc. The optical disc edge is quantified as R_{25} . Three parameters are considered: the sizes of HI disc with respect to the optical disc (R_{HI}/R_{25} , left panel), the fraction of total HI mass within the optical disc ($M_{\text{HI},r<R25}/M_{\text{HI}}$, middle panel), and the average HI surface density within the optical disc ($\Sigma_{\text{HI},r<R25}$, right panel). When the HI related parameter is defined with a radius smaller than $2 \times B_{\text{maj}}$ (the HI PSF size), the HI data is considered unresolved and the galaxy is excluded. In each panel, the correlation coefficient ρ is denoted on the left-top corner and the measurements error bar is shown in the right-top corner.

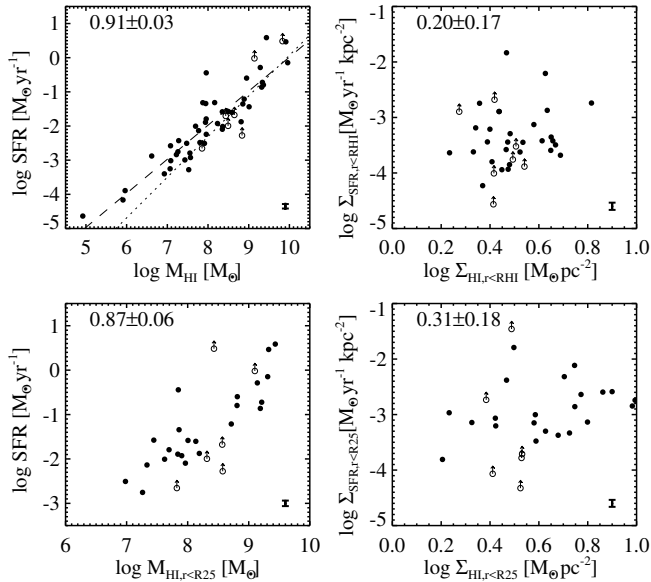


Figure 11. The relations between SFR and HI mass, and between their masses and surface densities within R_{25} . The open circles with an upward arrow mark the lower limits of SFE measurements for some galaxies; these data points are excluded when calculating the correlation coefficient ρ . When the HI related parameter is defined with a diameter smaller than $2B_{\text{maj}}$, the HI data is considered unresolved and the galaxy is excluded. The correlation coefficient is denoted on the top-left corner and the typical error bar is shown on the bottom-right corner of each panel. In the left-top panel, the dashed line is a linear fit to the data points (upper limits excluded), and the dotted line is the relation from [Huang et al. \(2012b\)](#).

slope is close to unity but with a large error bar, suggesting that it is hard to find any dependence of SFE on Σ_{HI} in our data.

The top-right panel shows that, as in irregular galaxies, there is also a trend of Σ_{SFR} to increase with higher Σ_* at $1.2R_{25}$. Which correlation might be more intrinsic? We

find that the partial correlation coefficient between Σ_{SFR} and Σ_{HI} with the effect of Σ_* removed is -0.22 ± 0.50 , while the partial correlation coefficient between Σ_{SFR} and Σ_* with the effect of Σ_{HI} removed is 0.84 ± 0.27 . The partial correlation analysis suggests that the $\Sigma_{\text{SFR}}-\Sigma_*$ correlation is more intrinsic than the $\Sigma_{\text{SFR}}-\Sigma_{\text{HI}}$ correlation and the latter is caused at least partly by the former.

To confirm this result, in the bottom panels of Figure 15, we further investigate the Σ_{SFR} correlations firstly at a fixed Σ_* of $3 M_{\odot} \text{pc}^{-2}$ and then at a fixed Σ_{HI} of $3 M_{\odot} \text{pc}^{-2}$. When $\Sigma_* = 3 M_{\odot} \text{pc}^{-2}$, Σ_{HI} ranges from $10^{0.49}$ to $10^{0.88} M_{\odot} \text{pc}^{-2}$, while when $\Sigma_{\text{HI}} = 3 M_{\odot} \text{pc}^{-2}$, Σ_* ranges from $10^{-0.20}$ to $10^{1.13} M_{\odot} \text{pc}^{-2}$. In these regions, Σ_* values are consistent with the value typical for HI-dominated regions, $\Sigma_* < 81 M_{\odot} \text{pc}^{-2}$ ([Leroy et al. 2008](#)). Σ_{HI} is close to the average surface density for transition between atomic and molecular gas ($5 M_{\odot} \text{pc}^{-2}$, with contribution from helium not included). However as shown in ([Leroy et al. 2008](#)) the atomic-to-molecular conversion is much more strongly correlated with Σ_* than with Σ_{HI} , hence most of these measurements are obtained from HI-dominated regions.

We find that there is a strong correlation of higher Σ_{SFR} with increasing Σ_* at a fixed $\Sigma_{\text{HI}} = 3 M_{\odot} \text{pc}^{-2}$, but very weak correlation between Σ_{SFR} and Σ_{HI} at a fixed $\Sigma_* = 3 M_{\odot} \text{pc}^{-2}$. This result implies that Σ_* is driving changes in Σ_{SFR} more dramatically than Σ_{HI} does in the galactic outskirts. These results are consistent with the finding from [Hunter et al. \(1998\)](#).

In the bottom panels of Figure 15, the dynamic range of Σ_* is greater than that of Σ_{HI} by nearly one dex for this sample. The wide dynamic range of Σ_* as well as the strong

³ Fixing surface densities at $3 M_{\odot} \text{pc}^{-2}$ rather than lower values comes from a compromise between limiting our analysis in the HI-dominated regions and the limited depth of the Σ_* data. If we use $2 M_{\odot} \text{pc}^{-2}$ instead of $3 M_{\odot} \text{pc}^{-2}$, the general trends do not change much but we will be at the risk of relying on extrapolated Σ_* values for more than half of the sample. If we use $4 M_{\odot} \text{pc}^{-2}$ instead of $3 M_{\odot} \text{pc}^{-2}$, we will be at the risk of reaching the molecular dominated high gas surface density regions.

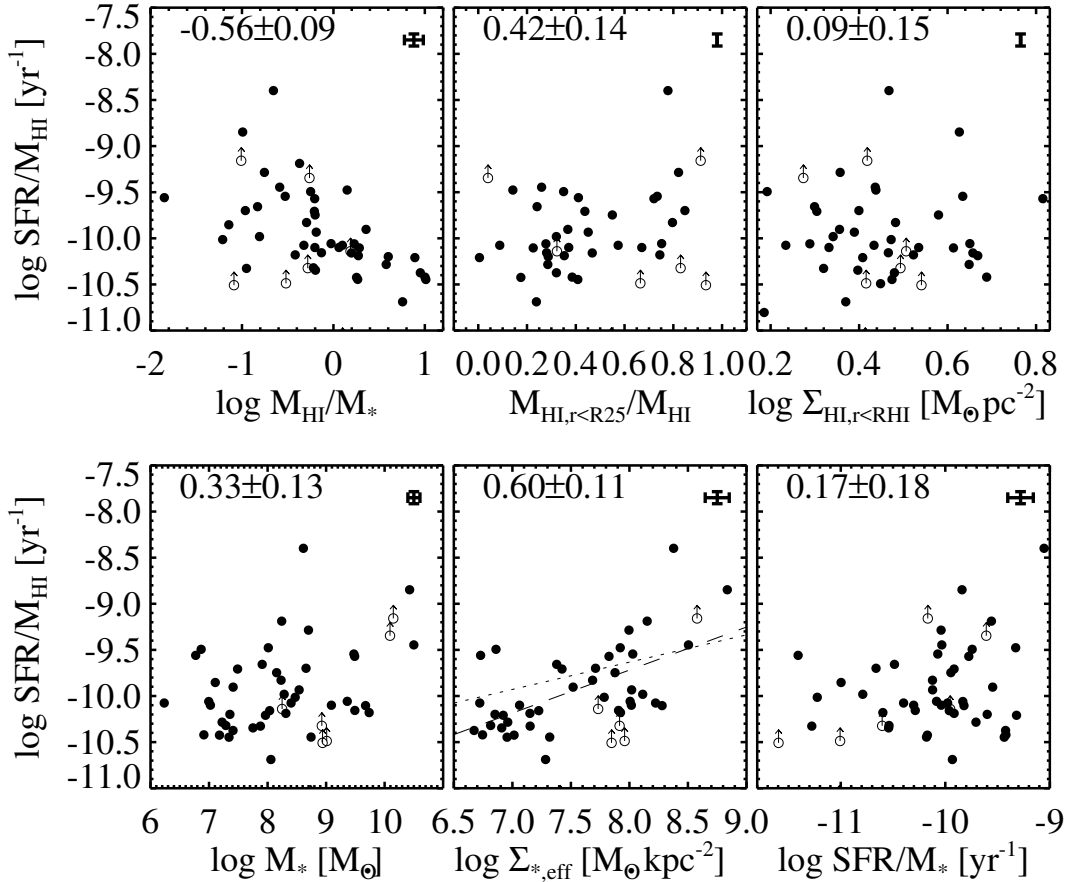


Figure 12. The dependence of global SFE on other galaxy properties. The open circles with an upper-ward arrow mark the lower limits of SFE measurements for some galaxies; these data points are excluded when calculating the correlation coefficient ρ . The correlation coefficient and typical error bar are shown in the corners of each panel. The dashed line in the bottom-middle panel is the robust linear fit to the data, and the dotted line is taken from [Wong et al. \(2016\)](#).

$\Sigma_{\text{SFR}}-\Sigma_*$ correlation have both contributed to producing the significant $\Sigma_{\text{SFR}}-\Sigma_{\text{HI}}$ correlation (without fixing Σ_*) shown in the top row of Figure 15.

We notice from all panels in Figure 15 the large scatter of Σ_{SFR} in the elliptical rings where each radial profile value is measured (the crosses in the figure). Limited by the variation in image resolutions in the sample and the small sample size, we can not evaluate how the scatter varies as a function of Σ_{HI} or Σ_* , but it can be inferred that the scatter in the $\Sigma_{\text{SFR}}-\Sigma_*$ relation might be as large as that in the $\Sigma_{\text{SFR}}-\Sigma_{\text{HI}}$ relation. The large scatter indicates complex physical factors other than the gravity provided by stars and HI gas that regulate star formation.

7.1.2 Analysis based on the radial measurements at the best possible resolution

For the second way of analysing the data, we use the radial profiles derived in Section 4.2.3. In addition to repeating the analysis in the bottom row of Figure 15, we further look into the dependence of Σ_{SFR} on Σ_* and σ_{sd} . σ_{sd} has been predicted by star formation models ([Ostriker et al. 2010](#); [Krumholz 2013](#)) to be a key parameter in setting the SFR in the outskirts of galaxies (see more details in Section 7.2). These results are presented in the top row of Figure 16. We

warn that we do not have a proper error estimate for Σ_* measured from the tilted ring models, and the estimate of σ_{sd} is based on simple assumptions.

From the left two panels in the top row of Figure 16, the trends are largely consistent with what we have found in the bottom panels of Figure 15. There is a moderate correlation between Σ_{SFR} and Σ_{HI} here, but it is significantly weaker than the $\Sigma_{\text{SFR}}-\Sigma_*$ correlation. In the last two panels of the top row, we also find significant correlations of Σ_{SFR} increasing as a function of σ_* and σ_{sd} . The slope for the $\Sigma_{\text{SFR}}-\sigma_{\text{sd}}$ relation is 1.07 ± 0.41 .

In the bottom row of Figure 16, we show the trends of SFE as function of Σ_{HI} , Σ_* , σ_* and σ_{sd} (defined at Section 4.2.3). SFE and Σ_{HI} are not correlated. The other trends are similar as the trends of Σ_{SFR} depending on those parameters.

We note that at $\Sigma_{\text{HI}} = 3 M_{\odot} \text{pc}^{-2}$, σ_{sd} is on average 3.5 times higher than σ_* in our sample, but the two volume densities correlate with each other with $\rho = 0.64 \pm 0.20$. Σ_* is correlated with σ_* ($\rho = 0.85 \pm 0.28$) because of the way it is calculated, but is not correlated with σ_{sd} ($\rho = 0.35 \pm 0.25$). The partial correlation between SFE and σ_* with the effect of σ_{sd} removed is 0.55 ± 0.45 , while the partial correlation between SFE and σ_{sd} with the effect of σ_* removed is 0.39 ± 0.48 . Hence the weak statistics does not allow us to

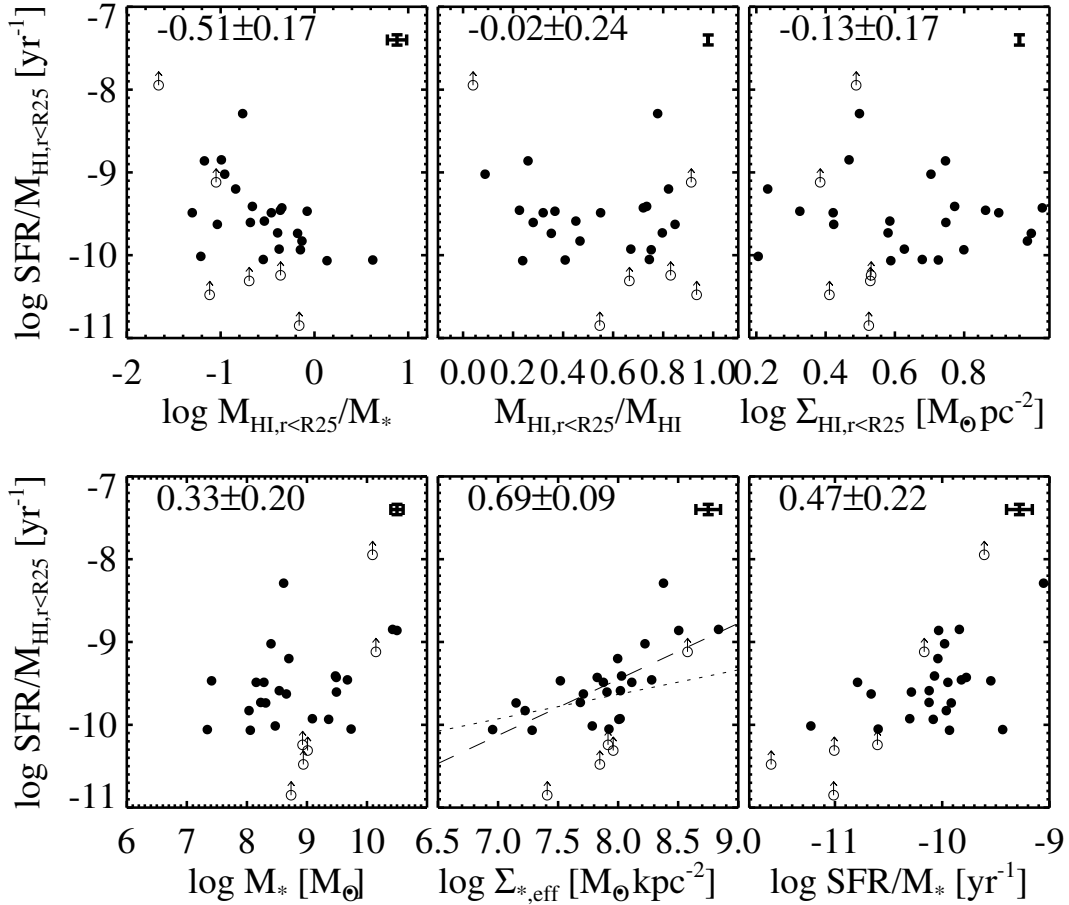


Figure 13. Similar as Figure 12, but all HI masses are measured within R_{25} . When the HI related parameter is defined with a diameter smaller than $2B_{maj}$, the HI data is considered unresolved and the galaxy is excluded.

conclude whether σ_{sd} or σ_* (Σ_*) has independent effects on setting SFE in the galactic outskirts. We will discuss it in more details in Section 7.3.

7.2 Comparison with existing observations

As we have mentioned, Bigiel et al. (2010) showed the Σ_{SFR} - Σ_{HI} relation for the outskirts of spiral discs. Σ_{SFR} and Σ_{HI} were measured in kpc-scale pixels, and the median relation has a power law slope of 1.7. Measuring the mean Σ_{SFR} in each Σ_{HI} bin instead, Roychowdhury et al. (2015) found a uniform power law slope between 1.4 and 1.7 for the relations between $\log \Sigma_{HI}$ and $\log \Sigma_{SFR}$ for irregular galaxies and the outskirts of spiral and massive disc galaxies. The non-unity slope suggests a correlation between $\log \Sigma_{HI}$ and \log SFE in the HI-dominated regime. On the other hand, Yıldız et al. (2017) only found a close-to-unity power law slope for the mean relation in the outskirts of early-type galaxies. When we derive the Σ_{SFR} - Σ_{HI} relation at $1.25 R_{25}$, we average over both star-forming and non-star-forming regions along the elliptical ring, but the power law slope of 1.24 ± 0.36 is consistent with the literature values within the error bar.

A large scatter in the Σ_{SFR} - Σ_{HI} relation has been shown in all these studies. In Bigiel et al. (2010), the distribution of Σ_{SFR} has a large scatter at a fixed Σ_{HI} (~ 1.5 dex at $\Sigma_{HI} = 1 M_{\odot} \text{ pc}^{-2}$). There is also large offset between the

median and mean values of Σ_{SFR} at a fixed Σ_{HI} (~ 0.5 dex at $\Sigma_{HI} = 1 M_{\odot} \text{ pc}^{-2}$) as revealed in Roychowdhury et al. (2015). Based on the FIGGS sample of irregular galaxies, Roychowdhury et al. (2009) found that each galaxy has its own slope and intercept for Σ_{SFR} - Σ_{HI} relation when such a correlation exists, while for 20% of the irregular galaxies (most of them disturbed) in their sample, Σ_{SFR} does not correlate with Σ_{HI} . The large scatter indicates complex physics regulating the relationship between SFR and HI gas.

Despite the uncertainty in slopes and the large scatter, the Σ_{SFR} - Σ_{HI} relations observed from these different studies (also see Yim & van der Hulst 2016) have one common feature: the inferred SFE is low and the gas depletion time is longer than the Hubble time.

As mentioned briefly in Section 1, the tight Σ_{SFR} - Σ_* relation was found for the HI-dominated irregular galaxies by Hunter et al. (1998). They tested a variety of physical quantities as possible regulators for star formation in irregular galaxies, including HI gas critical densities for gravity instabilities in different disc models. They found that only Σ_* correlates well with Σ_{SFR} along radial profiles in their investigation. In this paper, we find a strong Σ_{SFR} - Σ_* correlation also exist in the outskirts of spiral galaxies.

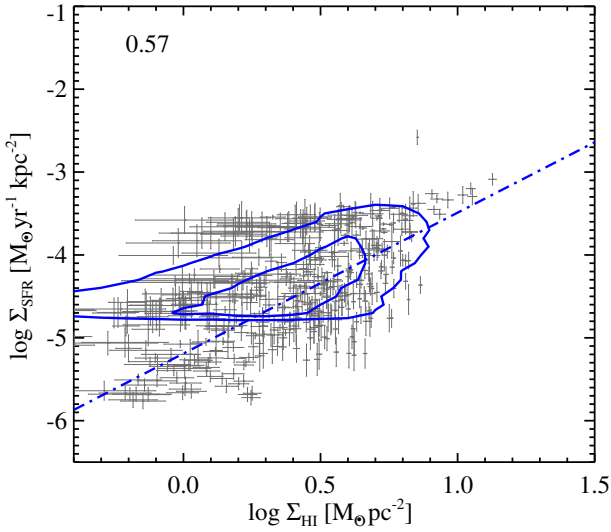


Figure 14. The dependence of Σ_{SFR} on Σ_{HI} . Measurements are derived from resolution-matched images. Σ_{HI} and Σ_{SFR} are measured in pixels with sizes equivalent to the PSF FWHM beyond R_{25} . We exclude those elements in which $\text{SFR} < 0.0003 M_{\odot} \text{ yr}^{-1}$, to avoid the problem of insufficient IMF sampling (Lee et al. 2009, 2011). The blue contours show the distribution of 50% and 90% of the data points, and the blue dot-dashed line show the median relation from Bigiel et al. (2010). Correlation coefficient ρ is denoted in the left-top corner.

7.3 Comparison with theoretical models

In this section we try to understand our results for the $\Sigma_{\text{SFR}}-\Sigma_{\text{HI}}$ and $\Sigma_{\text{SFR}}-\Sigma_{\star}$ relations in the context of modern star formation models.

Simple modern star formation models consider that 1) the atomic inter-stellar medium consists of a warm and a cold phase, and only the cold mode gas phase forms molecular clouds and stars; and that the 2) SFR in the HI-dominated regime is regulated by the hydrostatic equilibrium between thermal and dynamic pressure on gas at the mid-plane (Ostriker et al. 2010, O10 hereafter, Krumholz et al. 2013, K13 hereafter). The exact recipe for determining the pressure equilibrium between gas phases differs in different models. For example, in the O10 model, the atomic gas is in two-phase equilibrium everywhere and the thermal pressure is set by the radiation field and thus, it is a consequence of star formation feedback, while in the K13 model the cold phase density, sensitively depends on an assumed maximum temperature, above which the cold phase cannot exist. Other parameters of the model, such as the gas surface density and the SFR, are regulated under this condition.

In these models, the relation between the SFR and HI surface density are of complex nature. This is because, at the densities where HI dominates, other factors besides gravity contribute strongly to the equilibrium condition of the gas, such as temperature, sound speed, magnetic fields, cosmic rays and turbulence. K13 predicted a large scatter in the relation between Σ_{SFR} and Σ_{gas} (see their Figure 3 and Appendix A1). O10 predicted a complex dependence (their equation 22) of Σ_{SFR} as a function of Σ_{HI} , which contains several terms contributing equally. The large scatter and the

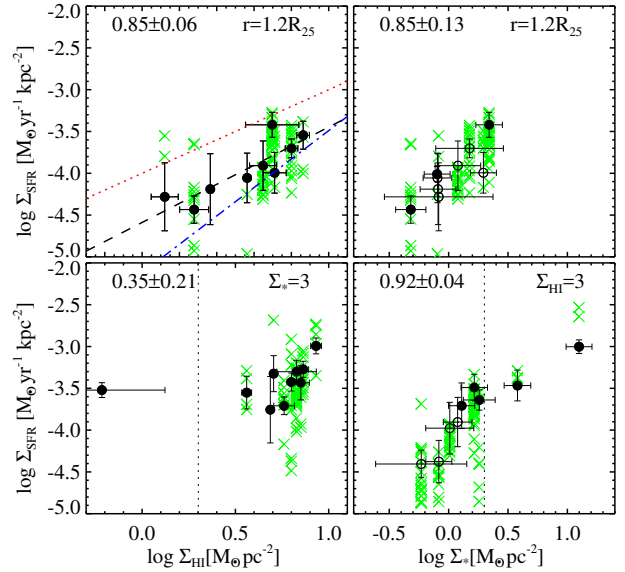


Figure 15. The dependence of Σ_{SFR} on Σ_{HI} and Σ_{\star} . Parameters are derived from resolution matched images. Only measurements with an error less than 0.5 dex are displayed and considered in the analysis. Solid and open circles are measurements derived from radial profiles. Solid circles mark direct measurements and open circles mark the Σ_{\star} measurements obtained through extrapolating radial profiles. Vertically from each circle, the green crosses show Σ_{SFR} measured in pixels with a size equivalent to the PSF FWHM (see Figure 14) along the elliptical ring where the radial profile value is measured. Due to the very different galactic sizes and image resolutions within the small sample, these crosses are only illustrative of the scatters in Σ_{SFR} along each elliptical ring and cannot be compared between different galaxies. In the top panels, data points are measured at $1.2R_{25}$. In the bottom-left panel, data points are measured on the elliptical ring where the averaged $\Sigma_{\star} = 3 M_{\odot} \text{ pc}^{-2}$; in the bottom-right panel, data points are measured along the elliptical ring where the average $\Sigma_{\text{HI}} = 3 M_{\odot} \text{ pc}^{-2}$. These characteristic positions are denoted in the top-right corner of each panel. The black dashed line is a linear fit to the data points, the blue dash-dotted line is the median relation from Bigiel et al. (2010), and the red dotted line marks an $\text{SFE} = 10^{10} \text{ yr}^{-1}$ or a gas depletion time of 10 Gyr. In the bottom panels, the black dotted lines mark the density of $3 M_{\odot} \text{ pc}^{-2}$. Correlation coefficient ρ is denoted in the left-top corner of each panel.

complex functional forms make it hard to constrain the models, because measuring the $\Sigma_{\text{HI}}-\Sigma_{\text{SFR}}$ relation from a small data set like LVHIS comes with observational uncertainties, and allow for significant ambiguity in the models.

Because old stars and dark matter contribute to the mid-plane pressure, both O10 and K13 models predict a SFR that increases with increasing σ_{sd} at a fixed gas density, which is what we observe in our data. Especially, the O10 model predicts $\Sigma_{\text{SFR}} \propto \sqrt{\sigma_{\text{sd}}}$ for the low gas surface density region (also see Kim et al. 2011). Our data reveal a power law index of 1.07 ± 0.41 , which does not necessarily disprove the O10 model, considering our crude calculation of the DM densities and the simplifications that go into the modelling. The $\Sigma_{\text{SFR}}-\sigma_{\text{sd}}$ relation also manifests itself as the $\Sigma_{\text{SFR}}-\Sigma_{\star}$ relation. Although the scatter in the $\Sigma_{\text{SFR}}-\Sigma_{\star}$ relation might be as large as that of the $\Sigma_{\text{SFR}}-\Sigma_{\text{HI}}$ relation given the same complex physical processes involved, the much wider dy-

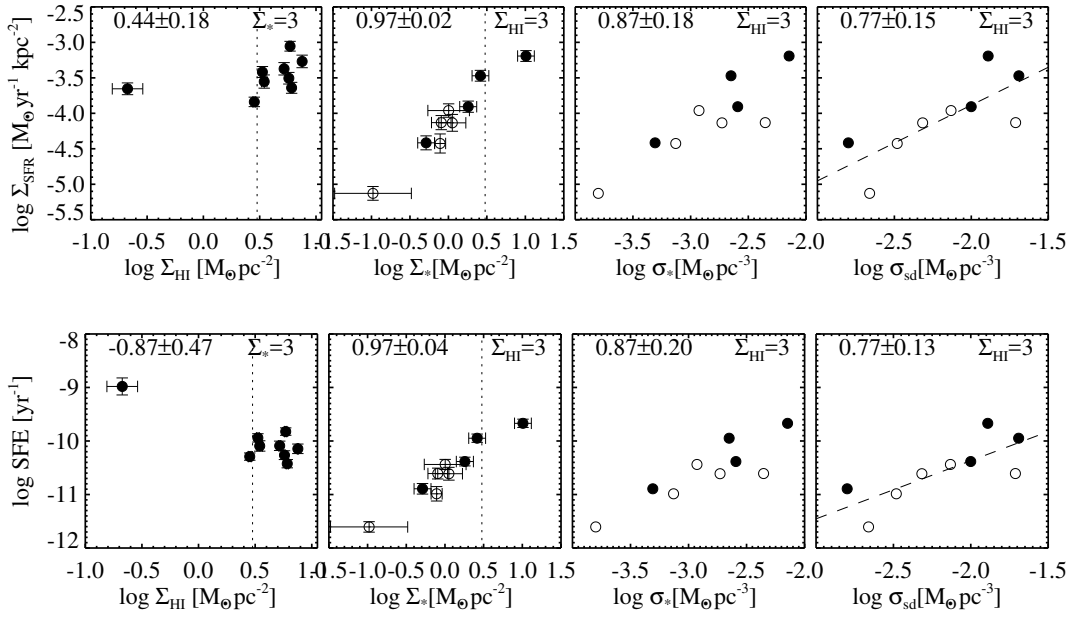


Figure 16. The dependence of Σ_{SFR} (top row) and SFE (bottom row) on Σ_{HI} , Σ_* , σ_* and σ_{sd} . Parameters are derived from GALEX and WISE images matched to the W4 resolution and tilted-ring fitting models. The dashed line in the top-right panel is a linear fit to the data points. Symbols, lines and denotes have the same meaning as in Figure 15.

dynamic range of Σ_* compared to Σ_{HI} has helped us to reveal a trend between Σ_* and Σ_{SFR} .

The $\Sigma_{\text{SFR}}-\Sigma_*$ relation might also partly reflect the SFE-metallicity relation (K13). Because metals are expected to provide the necessary shielding for star-forming clouds (Sternberg et al. 2014, and K13), and there is a strong correlation between Σ_* and local metallicity (Moran et al. 2012; Sánchez et al. 2013; Lara-López et al. 2013; Carton et al. 2015; Sánchez et al. 2017). Roychowdhury et al. (2015) found that the SFE in the outskirts of irregular and massive spiral galaxies are the same. Because irregular galaxies on average have much lower metallicity than the massive spiral galaxies, they concluded that the SFE in the galactic outskirts seem to be independent of metallicity. However, metallicities in the galactic outskirts might differ significantly from the global metallicities (Moran et al. 2012; Sánchez et al. 2012; López-Sánchez et al. 2015) which is what Roychowdhury et al. (2015) used for their analysis. Optical spectroscopy for the galactic outskirts is needed before we could make relevant conclusions, and we may need rely on the next generation IFU instruments like HECTOR (Bland-Hawthorn 2015).

In the past it has been suggested that star formation can have a positive feedback effect, effectively triggering more star formation (Gerola et al. 1980). In this picture, winds and the supernovae ejecta can cause gas compression at the shocks front, increasing the density of the gas and triggering new star formation. This is referred to as “self-propagation of star formation”, which seemingly could explain the $\Sigma_{\text{HI}}-\Sigma_*$ correlation. However, modern simulations Dale & Bonnell (2011); Dale et al. (2015) show that, although this form of positive feedback sometimes locally increases the gas density, enhancing star formation, the overall effect is negative. Ionising radiation effectively disperses low-to-intermediate mass molecular clouds while outflows disperse the more mas-

sive molecular clouds. In observations, there are examples of positive feedback at play and also a few of self-propagating (or subsequently triggered) star formation, such as the W5 HII region in the MW and the stellar cluster NGC 602 in the SMC (Koenig et al. 2008; Carlson et al. 2011). The conditions for self-propagating star formation to take place and whether this physical phenomenon could play an important role at low gas surface density regions (as predicted by Gerola et al. 1980) remains unclear.

To summarise, the strong $\Sigma_{\text{SFR}}-\Sigma_*$ correlation at a fixed Σ_{HI} and the relatively weak $\Sigma_{\text{SFR}}-\Sigma_{\text{HI}}$ correlation at a fixed Σ_* in the galactic outskirts are broadly consistent with modern star formation models. More detailed comparisons rely on more data points from larger samples in the future.

8 STAR FORMATION EFFICIENCY NEAR HI WARPS

We have shown in Section 4.2 that seven out of the ten LVHIS large galaxies display warped HI discs. Theoretical studies like that of Sánchez-Blázquez et al. (2009) have predicted a drop in SFE caused by the onset of an HI warp. Because SFE generally decreases with radius because of decreasing gas and stellar surface densities (Bigiel et al. 2010), we expect the additional effect from a warp would steepen the decrease. In this section, we investigate whether such a trend can be observed with our data.

We mark the warp radius r_{warp} on the SFE radial profiles in Figure 17. When calculating the SFE radial profiles, we derive Σ_{SFR} profiles at the resolution of the W4 images as in Section 4.2.3, but separate the approaching and receding velocity sides of a galaxy. We use Σ_{HI} profiles both directly derived from the mom-0 images and taken from the tilted-ring models. The former are less noisy and the latter

are better resolved, but they resulted in close SFE profiles as shown in Figure 17 because Σ_{HI} vary in a much narrower dynamic range than Σ_{SFR} .

We find the relations between HI warps, R_{25} and SFE radial profile shapes show great diversity within the very small sample. We summarise the most important results shown in Figure 17:

(i) r_{warp} is located close to R_{25} (with an offset $<0.3 R_{25}$) in most of the warped galaxies (6 out of 7). NGC 3621 has a warp that onsets extremely far away from the galactic centre: beyond $2.5 R_{25}$, and beyond the detection limit of our Σ_{SFR} data. In four out of the seven warped galaxies, r_{warp} on the two velocity sides differ by more than $0.4 R_{25}$ (NGC 55, NGC 3621 and NGC5236).

(ii) With the limited statistics available, there is no significant difference in the level of SFE beyond R_{25} between warped and un-warped galaxies.

(iii) Among the six HI warped galaxies where SFE is measurable at r_{warp} , the only case for r_{warp} to coincide with a steepened drop in SFE is in NGC 300. On the contrary, in NGC 55 and NGC 7793, r_{warp} coincides with the onset of a shallower SFE profile or even the turning over to a rising SFE profile. In other three warped galaxies, NGC 5236, IC 5052 and IC 5152, there are no clear signs that r_{warp} immediately coincides with a change in the slope of the SFE profile.

(iv) R_{25} shows a similar complex relation with SFE profile shapes as shown by r_{warp} .

In order to better quantify the relation between r_{warp} and change in SFE profile slope, we derive the second order derivative of SFE profiles near r_{warp} . For a given radius r , we first calculate the first order derivatives of SFE for the two radial segments with distances -0.25 to $0 R_{25}$ and 0 to $0.25 R_{25}$ from r , $\text{SFE}'_-(r)$ and $\text{SFE}'_+(r)$ respectively. And the second order derivative of SFE at r is calculated as $\text{SFE}''(r) = \text{SFE}'_+(r) - \text{SFE}'_-(r)$. For comparison, we also calculate SFE'' at R_{25} and at 100 random radii beyond R_{25} for each galaxy. All these calculations use SFE profiles measured at both the approaching and the receding velocity sides of galaxies. We use the SFE profiles with Σ_{HI} derived from HI column density images (the red and blue curves in Figure 17) in this analysis, but we have confirmed that, if we use the SFE profiles with Σ_{HI} derived from tilted ring models instead (the pink and cyan curves in Figure 17), the conclusion from the relevant results does not change.

Figure 18 shows that SFE'' measured at r_{warp} shows no significant difference with that measured at R_{25} or random radii beyond R_{25} . It confirms what we have visually summarised from Figure 17.

Hence what we learn from the limited statistics here is that we do not find strong evidence for HI warps to be *always* linked to suppressed SF activity. A larger sample from future HI surveys (WALLABY/Apertif, Koribalski 2012) is required to confirm this result or identify the possibly weak effect of warps.

9 SUMMARY AND CONCLUSION

We have analysed GALEX, WISE and HI images and characterised the HI M_* and SFR properties for galaxies in the

LVHIS sample. We use the resolved HI measurements to understand previously found global relations/trends (based on the LVHIS galaxies with $R_{25} > 2B_{\text{maj}}$) and investigate star formation properties in the galactic outskirts (beyond R_{25} , based on the ten large galaxies). We try to obtain a coherent picture of how SFR relates to the HI gas on different scales and in different regions. The major findings are:

(i) The HI radial distribution with respect to R_{25} is correlated with f_{HI} of galaxies (Figure 10). However the large scatter in the relations highlights the importance of using spatially resolved HI data to understand global relations.

(ii) The tight SFR- M_{HI} relation is caused by each being the product of galaxy area multiplying with Σ_{SFR} and Σ_{HI} , respectively, and does not reflect an intrinsic link between star formation and HI gas. The correlation between the globally averaged Σ_{SFR} and Σ_{HI} is weak (Figure 11). SFE significantly depends on the average stellar surface density $\Sigma_{*,\text{eff}}$, which was explained in Wong et al. (2016) with a marginally stable disc model.

(iii) The $\Sigma_{\text{SFR}}-\Sigma_{\text{HI}}$ correlation in the galactic outskirts becomes significantly weaker when Σ_* is fixed, while on the other hand there is a strong $\Sigma_{\text{SFR}}-\Sigma_*$ correlation at a fixed Σ_{HI} (Figure 15 and 16). These trends are consistent with star formation models where young stars are directly formed from the molecular gas, and are indirectly linked with HI gas through complex physical processes. In these models, old stars have a significant influence on the star formation process by providing gravity or through their link with metallicity.

(iv) HI warps hardly affect the SFE in the galactic outskirts (Figure 18).

These results suggest that the direct link between SFR and HI gas is generally weak in star forming galaxies. The SFR-HI relation measured globally and in the galactic outskirts are caused at least partly by side effects (both correlating to a third parameter, galaxy size for the former and Σ_* for the latter) and are intrinsically weaker than they appear to be. The gap between them and the (lack of) SFR-HI relations measured within galactic inner regions on kpc-scales (Bigiel et al. 2008) thus become much smaller. On the other hand, old stars may play a significant role in regulating star formation in both inner and outer regions of galaxies.

One major limitation of the analysis in this paper is the relatively small number of statistics, especially for the sub-sample of large galaxies. The relevant results will be strengthened by larger statistics, deeper images and follow-up optical spectroscopy. We look forward to high quality data and larger samples from future multi-wavelength surveys and instruments, such as WALLABY (Koribalski 2012), Skymapper (Keller et al. 2007) and HECTOR (Bland-Hawthorn 2015).

ACKNOWLEDGEMENTS

We thank the anonymous referee for constructive comments. We gratefully thank G. Muerer, M. Krumholz and B. Wang for useful discussions.

The HI 21-cm observations were obtained with the Australia Telescope Compact Array which is funded by the

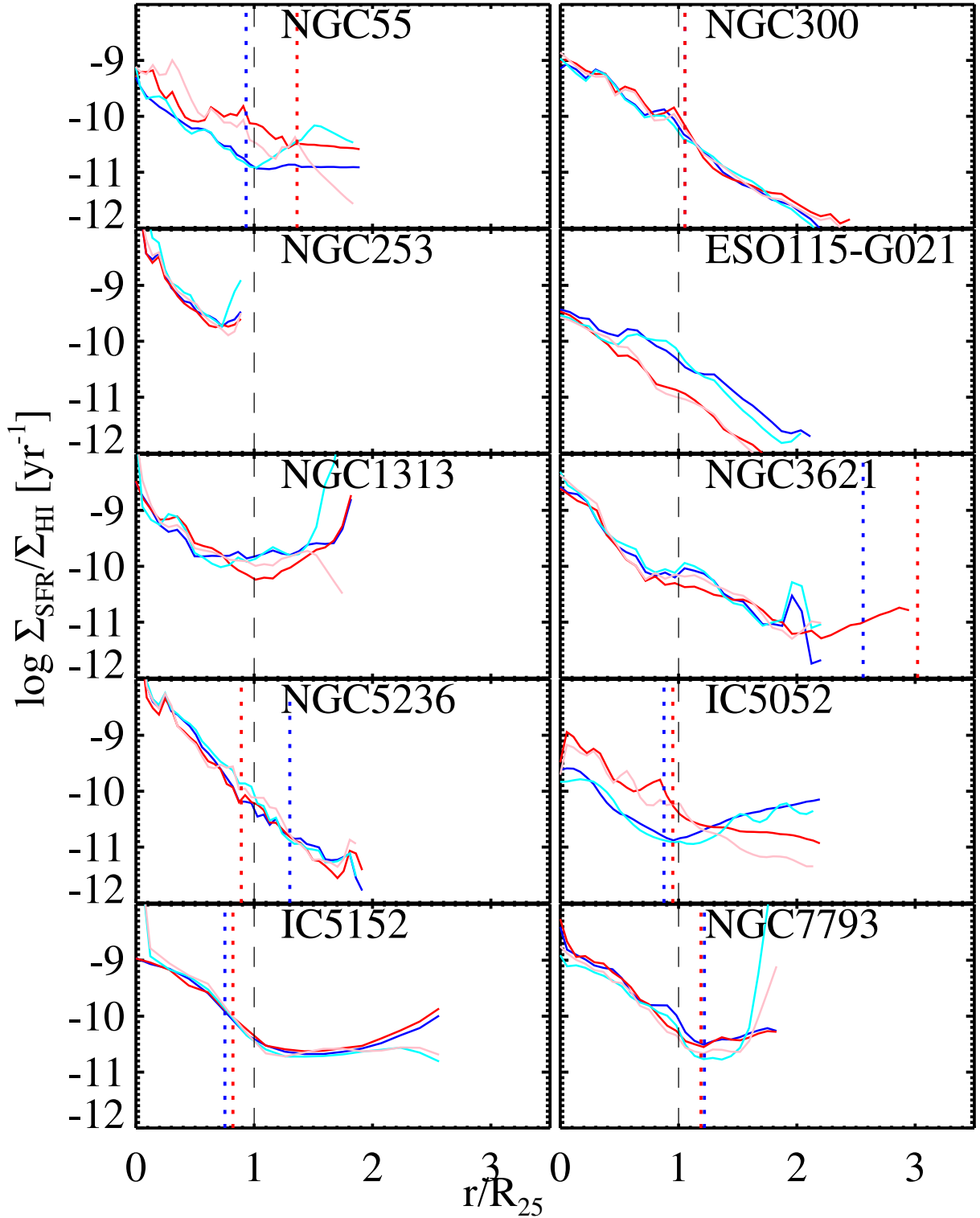


Figure 17. The SFE radial profiles for the ten well-resolved LVHIS galaxies. The blue and red solid curves show SFE calculated for the approaching and receding sides of the galaxy respectively, with Σ_{HI} derived from HI column density images. The cyan and pink solid curves show SFE calculated for the approaching and receding velocity sides of the galaxy respectively, with Σ_{HI} taken from the tilted ring models. The blue and red dotted lines mark r_{warp} on the approaching and receding velocity sides respectively, when an HI warp exists (Section 2). The radius is normalised by R_{25} . The black dashed lines mark R_{25} .

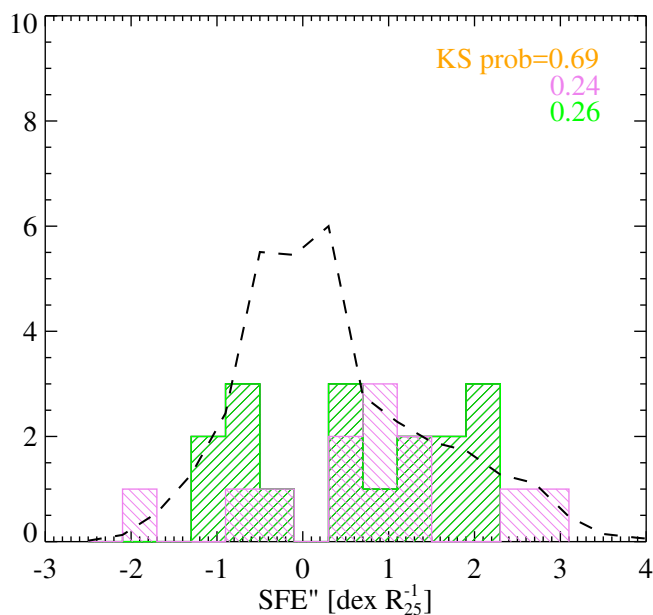


Figure 18. The distributions of second order derivatives of SFE measured at r_{warp} (violet), R_{25} (green) and random radii (r_{random}) beyond R_{25} (black). The black histogram has been normalised to have comparable height as the violet and green histograms. The top right corner shows the Kolmogorov-Smirnov (KS) test probabilities for the null hypothesis that the two distributions are drawn from the same parental distribution. The numbers in orange, violet and green show the KS test probabilities for the comparisons $SFE''(r_{warp})$ vs $SFE''(R_{25})$, $SFE''(r_{warp})$ vs $SFE''(r_{random})$ and $SFE''(R_{25})$ vs $SFE''(r_{random})$ respectively.

Commonwealth of Australia for operations as a National Facility managed by CSIRO.

GALEX (Galaxy Evolution Explorer) is a NASA Small Explorer, launched in April 2003, developed in cooperation with the Centre National d'Études Spatiales of France and the Korean Ministry of Science and Technology.

This publication makes use of data products from the Wide-field Infrared Survey Explorer, which is a joint project of the University of California, Los Angeles, and the Jet Propulsion Laboratory/California Institute of Technology, funded by the National Aeronautics and Space Administration.

This research has made use of the SIMBAD database¹, operated at CDS, Strasbourg, France.

ZYL is supported by the National Natural Science Foundation of China under grant no. 11403072, by the China-Chile joint grant from CASSACA, and by Shanghai Yangfan Research Grant (no. 14YF1407700).

The work of LCH was supported by National Key Program for Science and Technology Research and Development grant 2016YFA0400702.

JMvdH acknowledges support from the European Research Council under the European Unions Seventh Framework Programme (FP/2007-2013)/ERC Grant Agreement no. 291531.

This project has received funding from the European

Research Council (ERC) under the European Union's Horizon 2020 research and innovation programme (grant agreement no. 679627).

REFERENCES

- Aniano G., Draine B. T., Gordon K. D., Sandstrom K., 2011, *PASP*, **123**, 1218
- Bakos J., Trujillo I., Pohlen M., 2008, *ApJ*, **683**, L103
- Begum A., Chengalur J. N., Karachentsev I. D., Sharina M. E., Kaisin S. S., 2008, *MNRAS*, **386**, 1667
- Bell E. F., McIntosh D. H., Katz N., Weinberg M. D., 2003, *ApJS*, **149**, 289
- Bertin E., Arnouts S., 1996, *A&AS*, **117**, 393
- Bigiel F., Leroy A., Walter F., Brinks E., de Blok W. J. G., Madore B., Thornley M. D., 2008, *AJ*, **136**, 2846
- Bigiel F., Leroy A., Walter F., Blitz L., Brinks E., de Blok W. J. G., Madore B., 2010, *AJ*, **140**, 1194
- Bland-Hawthorn J., 2015, in Ziegler B. L., Combes F., Dannerbauer H., Verdugo M., eds, IAU Symposium Vol. 309, Galaxies in 3D across the Universe. pp 21–28 ([arXiv:1410.3838](https://arxiv.org/abs/1410.3838)), [doi:10.1017/S1743921314009247](https://doi.org/10.1017/S1743921314009247)
- Boselli A., Cortese L., Boquien M., 2014, *A&A*, **564**, A65
- Briggs F. H., 1990, *ApJ*, **352**, 15
- Brown M. J. I., et al., 2014, *ApJS*, **212**, 18
- Brown T., Catinella B., Cortese L., Kilborn V., Haynes M. P., Giovanelli R., 2015, *MNRAS*, **452**, 2479
- Calzetti D., 2013, Star Formation Rate Indicators. p. 419
- Carlson L. R., et al., 2011, *ApJ*, **730**, 78
- Carton D., et al., 2015, *MNRAS*, **451**, 210
- Catinella B., et al., 2010, *MNRAS*, **403**, 683
- Catinella B., et al., 2013, *MNRAS*, **436**, 34
- Cluver M. E., et al., 2014, *ApJ*, **782**, 90
- Contursi A., et al., 2002, *AJ*, **124**, 751
- Cortese L., et al., 2012, *A&A*, **544**, A101
- Cutri R. M., et al., 2012, Technical report, Explanatory Supplement to the WISE All-Sky Data Release Products
- Dale J. E., Bonnell I., 2011, *MNRAS*, **414**, 321
- Dale D. A., et al., 2009, *ApJ*, **703**, 517
- Dale J. E., Haworth T. J., Bressert E., 2015, *MNRAS*, **450**, 1199
- Dutton A. A., van den Bosch F. C., Dekel A., 2010, *MNRAS*, **405**, 1690
- Elbaz D., et al., 2007, *A&A*, **468**, 33
- García-Ruiz I., Sancisi R., Kuijken K., 2002, *A&A*, **394**, 769
- Gerola H., Seiden P. E., Schulman L. S., 1980, *ApJ*, **242**, 517
- Giovanelli R., et al., 2005, *AJ*, **130**, 2598
- Grootes M. W., et al., 2013, *ApJ*, **766**, 59
- Hao C.-N., Kennicutt R. C., Johnson B. D., Calzetti D., Dale D. A., Moustakas J., 2011, *ApJ*, **741**, 124
- Ho L. C., Li Z.-Y., Barth A. J., Seigar M. S., Peng C. Y., 2011, *ApJS*, **197**, 21
- Huang S., Haynes M. P., Giovanelli R., Brinchmann J., Stierwalt S., Neff S. G., 2012a, *AJ*, **143**, 133
- Huang S., Haynes M. P., Giovanelli R., Brinchmann J., 2012b, *ApJ*, **756**, 113
- Hunter D. A., Elmegreen B. G., 2006, *ApJS*, **162**, 49
- Hunter D. A., Elmegreen B. G., Baker A. L., 1998, *ApJ*, **493**, 595
- Hunter D. A., et al., 2012, *AJ*, **144**, 134
- Jarrett T. H., et al., 2012, *AJ*, **144**, 68
- Jarrett T. H., et al., 2013, *AJ*, **145**, 6
- Jarrett T. H., et al., 2016, preprint, ([arXiv:1607.01190](https://arxiv.org/abs/1607.01190))
- Johnson M. C., et al., 2015, *MNRAS*, **451**, 3192
- Józsa G. I. G., 2007, *A&A*, **468**, 903
- Józsa G. I. G., Kenn F., Klein U., Oosterloo T. A., 2007, *A&A*, **468**, 731

¹ <http://simbad.u-strasbg.fr/simbad/>

- Kamphuis P., Józsa G. I. G., Oh S.-H., Spekkens K., Urbancic N., Serra P., Koribalski B. S., Dettmar R.-J., 2015, *MNRAS*, **452**, 3139
- Keller S. C., et al., 2007, *PASA*, **24**, 1
- Kennicutt Jr. R. C., Lee J. C., Funes J. G., J. S., Sakai S., Akiyama S., 2008, *ApJS*, **178**, 247
- Kim C.-G., Kim W.-T., Ostriker E. C., 2011, *ApJ*, **743**, 25
- Kirby E. M., Koribalski B., Jerjen H., López-Sánchez Á., 2012, *MNRAS*, **420**, 2924
- Koenig X. P., Allen L. E., Gutermuth R. A., Hora J. L., Brunt C. M., Muzerolle J., 2008, *ApJ*, **688**, 1142
- Koribalski B. S., 2012, *PASA*, **29**, 359
- Koribalski B. S., López-Sánchez Á. R., 2009, *MNRAS*, **400**, 1749
- Koribalski B. S., et al., 2004, *AJ*, **128**, 16
- Kroupa P., 2001, *MNRAS*, **322**, 231
- Krumholz M. R., 2013, *MNRAS*, **436**, 2747
- Lara-López M. A., et al., 2013, *MNRAS*, **433**, L35
- Lauberts A., Valentijn E. A., 1989, The surface photometry catalogue of the ESO-Uppsala galaxies
- Lee J. C., et al., 2009, *ApJ*, **706**, 599
- Lee J. C., et al., 2011, *ApJS*, **192**, 6
- Leroy A. K., Walter F., Brinks E., Bigiel F., de Blok W. J. G., Madore B., Thornley M. D., 2008, *AJ*, **136**, 2782
- Li Z.-Y., Ho L. C., Barth A. J., Peng C. Y., 2011, *ApJS*, **197**, 22
- López-Sánchez Á. R., Koribalski B. S., van Eymeren J., Esteban C., Kirby E., Jerjen H., Lonsdale N., 2012, *MNRAS*, **419**, 1051
- López-Sánchez Á. R., Westmeier T., Esteban C., Koribalski B. S., 2015, *MNRAS*, **450**, 3381
- Martin D. C., et al., 2005, *ApJ*, **619**, L1
- Masci F., 2013, ICORE: Image Co-addition with Optional Resolution Enhancement, Astrophysics Source Code Library (ascl:1302.010)
- McClure-Griffiths N. M., et al., 2009, *ApJS*, **181**, 398
- Meurer G. R., et al., 2006, *ApJS*, **165**, 307
- Meyer M. J., et al., 2004, *MNRAS*, **350**, 1195
- Moran S. M., et al., 2012, *ApJ*, **745**, 66
- Morrissey P., et al., 2007, *ApJS*, **173**, 682
- Noeske K. G., et al., 2007, *ApJ*, **660**, L43
- Ostriker E. C., McKee C. F., Leroy A. K., 2010, *ApJ*, **721**, 975
- Overzier R. A., et al., 2011, *ApJ*, **726**, L7
- Pohlen M., Trujillo I., 2006, *A&A*, **454**, 759
- Polletta M. d. C., et al., 2006, *ApJ*, **642**, 673
- Polletta M., et al., 2007, *ApJ*, **663**, 81
- Renzini A., Peng Y.-j., 2015, *ApJ*, **801**, L29
- Roychowdhury S., Chengalur J. N., Begum A., Karachentsev I. D., 2009, *MNRAS*, **397**, 1435
- Roychowdhury S., Chengalur J. N., Kaisin S. S., Karachentsev I. D., 2014, *MNRAS*, **445**, 1392
- Roychowdhury S., Huang M.-L., Kauffmann G., Wang J., Chengalur J. N., 2015, *MNRAS*, **449**, 3700
- Saintonge A., et al., 2016, *MNRAS*, **462**, 1749
- Sánchez-Blázquez P., Courty S., Gibson B. K., Brook C. B., 2009, *MNRAS*, **398**, 591
- Sánchez S. F., et al., 2012, *A&A*, **546**, A2
- Sánchez S. F., et al., 2013, *A&A*, **554**, A58
- Sánchez S. F., et al., 2017, preprint, ([arXiv:1703.09769](https://arxiv.org/abs/1703.09769))
- Schiminovich D., et al., 2010, *MNRAS*, **408**, 919
- Silva L., Granato G. L., Bressan A., Danese L., 1998, *ApJ*, **509**, 103
- Stanimirovic S., 2002, in Stanimirovic S., Altschuler D., Goldsmith P., Salter C., eds, *Astronomical Society of the Pacific Conference Series Vol. 278, Single-Dish Radio Astronomy: Techniques and Applications*. pp 375–396 ([arXiv:astro-ph/0205329](https://arxiv.org/abs/astro-ph/0205329))
- Sternberg A., Le Petit F., Roueff E., Le Bourlot J., 2014, *ApJ*, **790**, 10
- Swaters R. A., Balcells M., 2002, *A&A*, **390**, 863
- Swaters R. A., van Albada T. S., van der Hulst J. M., Sancisi R., 2002, *A&A*, **390**, 829
- Teich Y. G., et al., 2016, *ApJ*, **832**, 85
- Walter F., Brinks E., de Blok W. J. G., Bigiel F., Kennicutt Jr. R. C., Thornley M. D., Leroy A., 2008, *AJ*, **136**, 2563
- Wang J., Overzier R., Kauffmann G., von der Linden A., Kong X., 2010, *MNRAS*, **401**, 433
- Wang J., Koribalski B. S., Serra P., van der Hulst T., Roychowdhury S., Kamphuis P., Chengalur J. N., 2016, *MNRAS*, **460**, 2143
- Wenger M., et al., 2000, *A&AS*, **143**, 9
- Whitaker K. E., van Dokkum P. G., Brammer G., Franx M., 2012, *ApJ*, **754**, L29
- Wong O. I., Meurer G. R., Zheng Z., Heckman T. M., Thilker D. A., Zwaan M. A., 2016, *MNRAS*, **460**, 1106
- Wright E. L., et al., 2010, *AJ*, **140**, 1868
- Yıldız M. K., Serra P., Peletier R. F., Oosterloo T. A., Duc P.-A., 2017, *MNRAS*, **464**, 329
- Yim K., van der Hulst J. M., 2016, *MNRAS*, **463**, 2092
- Young T., Jerjen H., López-Sánchez Á. R., Koribalski B. S., 2014, *MNRAS*, **444**, 3052
- van Eymeren J., Koribalski B. S., López-Sánchez Á. R., Dettmar R.-J., Bomans D. J., 2010, *MNRAS*, **407**, 113
- van der Kruit P. C., 2007, *A&A*, **466**, 883

APPENDIX A: MEASUREMENTS TABLES

GALEX and WISE photometric measurements for LVHIS galaxies are presented in Tables A1 and A2 respectively.

Table A1 gives the fitted FUV and NUV scale-length of the outer disc (r_s), the apparent magnitude corrected for foreground extinction (m), the effective radius that enclose half of the light (r_{eff}) and the effective surface brightness (the average brightness within r_{eff} , μ_{eff}). See Section 3.1 for details.

Table A2 the four WISE band luminosities ($\log L_{W1-4}$), the W1-W2 colour and the W1 structural parameters. The superscript f marks the galaxies not detected in the W2-band, for which we have enforced the W1 aperture on the W2 images in order to measure the W2 fluxes. The expected (model) stellar continuum are removed from the luminosities $\log L_{W3}$ and $\log L_{W4}$. The W1 in-band luminosity ($L_{W1,\odot}$) is normalised by the equivalent solar value and used for calculating stellar mass-to-light ratio. R_{75} and R_{25} are the 75% and 25% light radius and the ratio between the two is a measure of the central concentration. See Section 3.2 for details.

APPENDIX B: ATLAS OF THE LARGE GALAXIES

In Figure B1 we present the resolution-matched distributions of M_* , SFR and M_{HI} (left side) and radial SB profiles (right side) for the ten large LVHIS galaxies (see Section 4.1 and 7). Ellipses in the images and vertical lines in the SB profile figures mark three radii, at $1.25 R_{25}$ (dotted), $\Sigma_* = 3 M_{\odot} \text{pc}^{-2}$ (dashed), and $\Sigma_{\text{HI}} = 3 M_{\odot} \text{pc}^{-2}$ (dash-dotted), which are also annotated with star symbols in the Σ_* and Σ_{HI} profiles.

In Figure B2 we present images for the same sample of 10 large LVHIS galaxies showing the distribution of M_* (at the resolution of the WISE W1-band), SFR (at the resolution of the WISE W4-band), and the mean ATCA HI

Table A1. GALEX photometric measurements for the LVHIS galaxies.

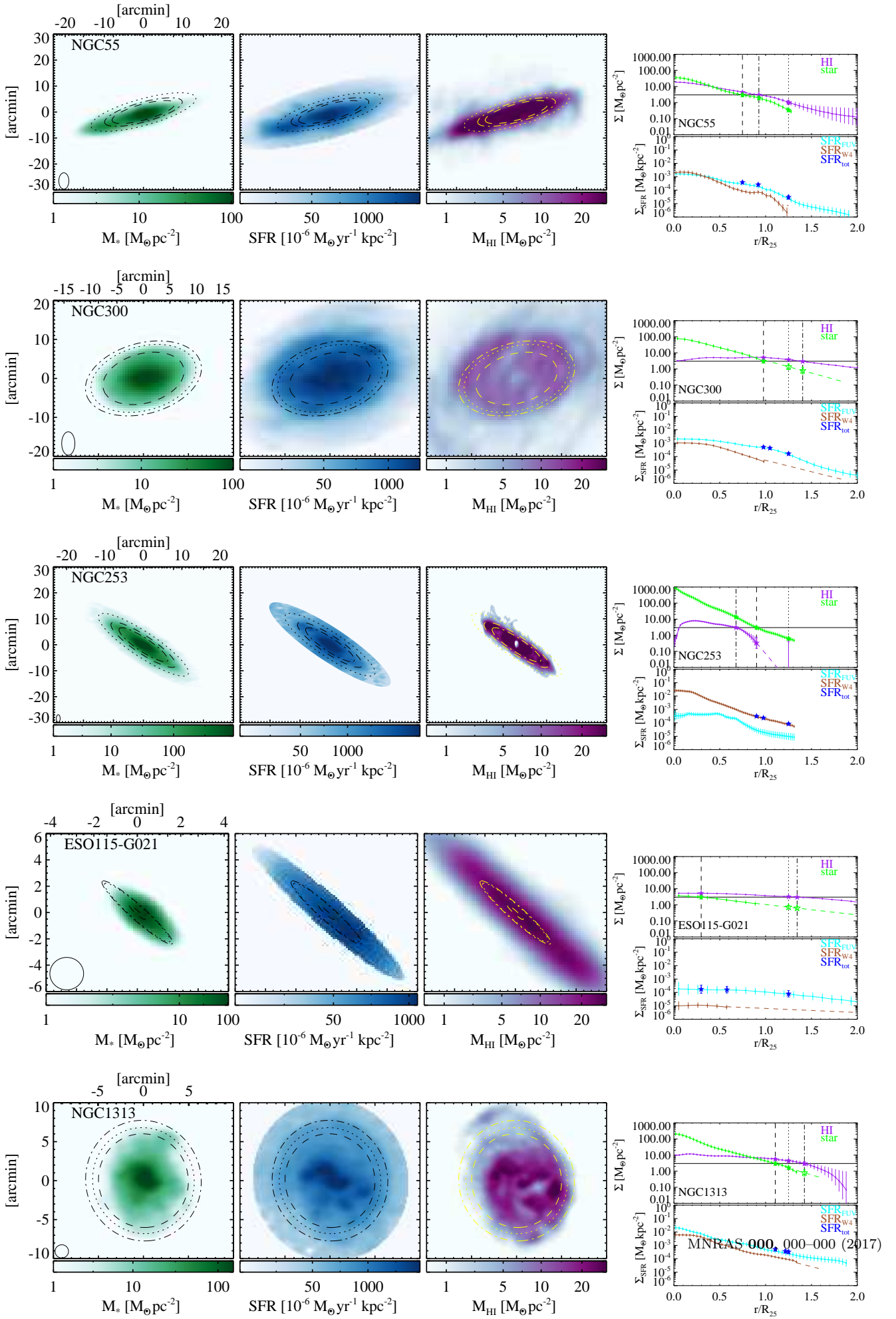
IDs index	FUV				NUV			
	r_s arcsec (2)	m mag (3)	r_{eff} arcsec (4)	μ_{eff} mag arcsec ⁻² (5)	r_s arcsec (6)	m mag (7)	r_{eff} arcsec (8)	μ_{eff} mag arcsec ⁻² (9)
1	8.1±0.4	17.16±0.06	9.1	27.55	8.6±0.5	16.97±0.03	10.1	24.03
2	33.7±7.1	17.67±0.58	8.0	28.43	20.0±1.0	17.58±0.03	6.4	23.68
3	8.5±1.1	18.33±0.11	13.5	28.67	13.6±0.4	17.26±0.04	8.7	24.01
4	128.6±0.1	10.31±0.05	111.9	20.67	121.0±0.1	9.92±0.03	107.7	22.08
5	206.6±9.0	10.31±0.05	130.5	20.66	177.3±13.7	10.10±0.03	120.1	22.49
6	227.4±0.8	11.24±0.05	160.5	21.59	256.3±0.5	10.63±0.03	167.0	23.74
7	145.9±5.1	11.47±0.05	161.3	21.82	208.9±10.6	11.18±0.03	132.9	23.79
8	97.2±7.0	13.79±0.05	3.0	24.14	108.4±3.8	13.30±0.03	3.4	17.95
9	27.8±0.7	13.74±0.05	28.2	24.10	29.1±1.0	13.61±0.03	27.8	22.83
10	62.1±20.1	16.21±0.07	42.5	26.52	72.8±2.7	15.01±0.03	32.9	24.66
11	46.4±0.3	14.68±0.05	38.0	25.04	47.6±0.3	14.40±0.03	37.3	24.26
12	38.1±0.2	13.89±0.05	48.5	24.25	39.4±0.1	13.70±0.03	44.6	23.94
13	6.1±0.6	17.69±0.24	10.0	28.06	6.6±0.5	17.58±0.08	10.0	24.60
14	112.3±3.4	10.52±0.05	50.8	20.89	79.1±1.8	10.37±0.03	44.8	20.63
15	20.9±0.5	14.81±0.05	13.1	25.16	30.4±2.3	14.46±0.03	12.3	21.91
16	13.4±3.9	19.23±1.00	21.2	28.75	9.7±1.8	18.90±1.13	18.1	27.20
17	22.0±0.6	14.48±0.05	27.2	24.82	50.3±3.7	14.25±0.03	18.6	22.59
18	60.6±1.5	13.40±0.05	-	-	78.6±4.3	13.45±0.03	-20.4	21.99
19	-	-	-	-	35.9±2.9	15.26±0.05	11.6	22.59
23	9.1±0.3	16.62±0.13	8.6	26.93	8.4±1.9	16.43±0.08	10.4	23.49
27	24.3±3.0	13.38±0.05	12.2	23.71	87.7±3.5	12.97±0.03	-1.1	15.28
28	-	-	-	-	7.3±0.4	15.74±0.07	6.6	21.89
29	16.4±1.1	16.17±0.27	13.2	26.57	17.1±0.6	15.90±0.09	13.6	23.59
30	128.4±6.2	13.49±0.05	102.3	23.82	164.6±2.4	12.94±0.03	99.3	24.92
31	157.4±0.8	11.66±0.05	123.8	22.03	377.8±8.5	11.09±0.03	57.3	21.87
32	1.6±0.3	18.81±0.10	-	-	4.5±0.4	18.08±1.07	8.6	24.89
33	-	-	-	-	9.4±0.4	17.89±0.40	18.8	25.97
34	20.1±36.5	17.85±1.83	-	-	5.3±1.2	17.80±0.47	15.6	25.55
36	-	-	-	-	6.0±1.1	17.21±1.77	11.9	24.93
37	11.4±1.1	16.55±0.06	12.9	26.90	20.5±2.3	16.14±0.03	9.5	23.03
40	27.2±1.5	15.21±0.06	25.2	25.51	25.7±1.2	14.90±0.03	24.1	23.78
42	11.2±4.4	17.29±0.31	15.3	27.57	7.6±1.3	17.34±0.09	12.4	24.71
44	7.4±1.4	16.28±0.18	13.0	26.47	26.7±2.3	14.97±0.09	10.0	21.96
45	10.2±1.4	18.28±0.17	14.2	28.65	24.0±2.5	17.64±0.04	8.5	24.33
47	5.4±2.3	18.33±1.65	12.5	28.62	10.3±1.9	17.43±0.91	17.3	25.67
48	149.0±14.4	11.81±0.05	66.6	22.12	227.5±0.5	10.86±0.03	70.8	22.12
49	7.0±0.1	16.05±0.05	7.8	26.39	21.2±1.9	15.56±0.03	5.5	21.24
50	18.1±0.9	14.17±0.08	51.9	24.43	31.7±0.4	13.94±0.03	20.3	22.50
52	8.0±1.6	17.58±0.22	18.2	27.89	20.0±0.9	16.52±0.12	11.5	23.97
53	185.7±38.1	10.14±0.05	74.5	20.49	327.0±1.6	9.54±0.03	46.3	19.86
54	4.9±0.9	17.23±1.60	13.1	27.56	7.4±0.3	16.96±0.12	9.3	23.79
55	8.5±2.3	15.42±0.17	10.1	25.82	35.4±10.2	14.59±0.05	9.9	21.39
56	8.4±0.3	16.09±0.05	27.5	26.37	129.5±54.7	15.67±0.03	9.5	22.55
57	224.8±14.4	12.39±0.05	-	-	139.1±2.1	11.91±0.03	-17.4	20.10
58	6.5±0.5	16.17±0.07	4.4	26.53	9.2±0.6	15.88±0.05	4.5	21.18
59	136.5±30.1	14.79±0.06	9.2	25.17	66.2±7.8	14.34±0.03	11.7	21.70
74	-	-	-	-	29.9±2.8	13.30±0.06	25.7	22.36
75	200.8±1.6	12.02±0.05	22.6	22.43	305.4±12.1	12.10±0.03	-50.9	22.58
77	134.7±12.8	13.99±0.05	35.3	24.34	92.1±4.6	13.48±0.03	34.8	23.18
78	140.0±7.9	12.55±0.05	21.8	22.91	107.3±1.5	12.21±0.03	20.4	20.75
79	57.4±4.7	15.39±0.06	11.4	25.75	82.3±7.9	14.88±0.04	10.0	22.03
80	23.2±0.4	14.89±0.05	24.1	25.25	25.0±0.3	14.69±0.03	22.4	23.44
81	21.3±0.5	15.69±0.05	11.8	26.06	21.5±0.3	15.65±0.03	13.3	23.28
82	131.7±1.7	11.23±0.05	67.8	21.58	217.9±3.3	10.98±0.03	46.9	21.33

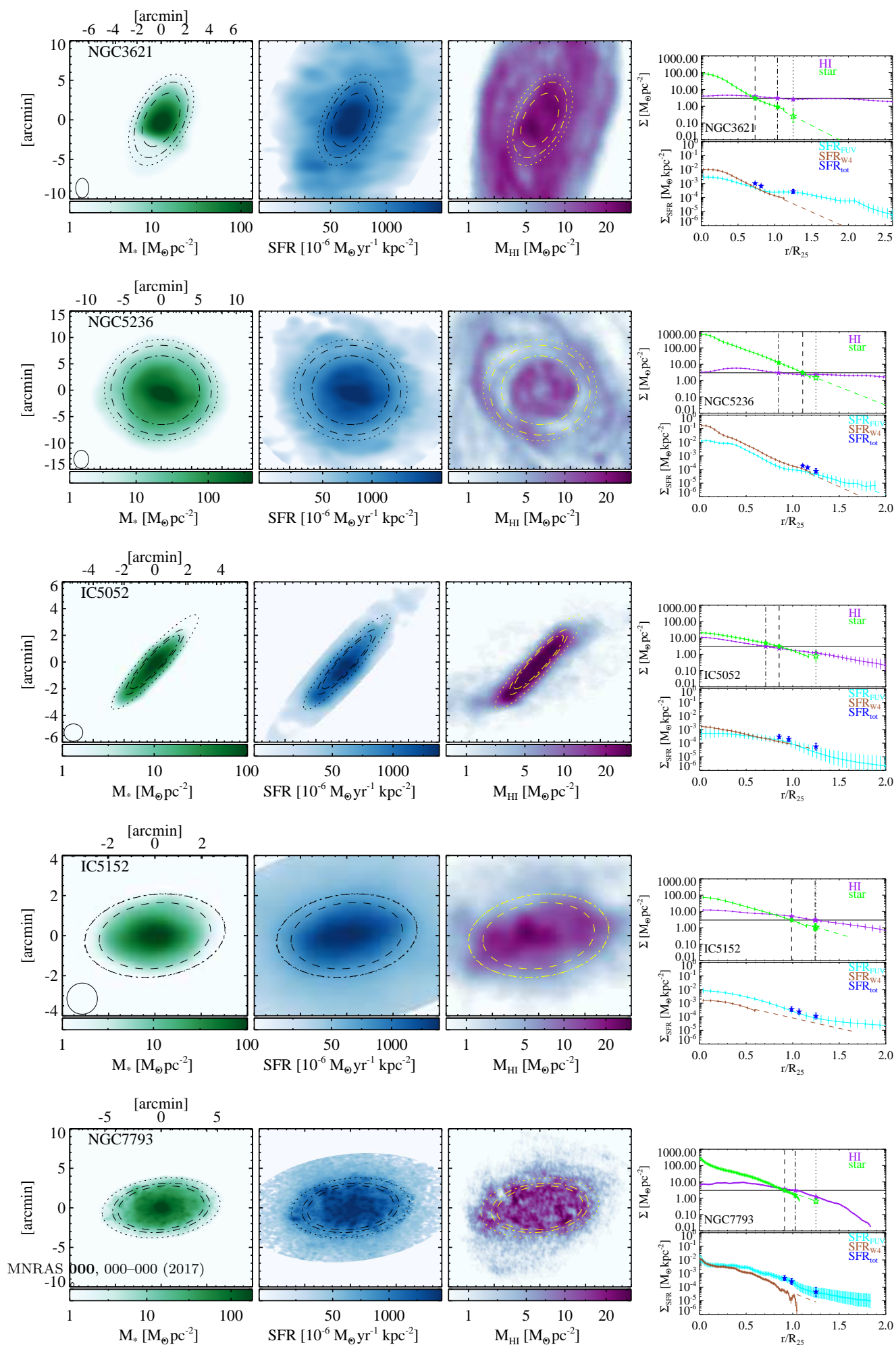
velocity field at the original resolution (left side) as well as our tilted ring models and derived tiltograms (right side). Ellipses in the images highlight the onset of the warp (r_{warp} , solid line), if present, and the R_{25} isophote (dashed line). For each tilted ring model we show from top to bottom the rotational velocity (v_{rot}), position angle (PA), inclina-

tion angle (i) and HI surface brightness (Σ_{HI}) as a function of radius. The approaching, receding and mean values are coloured in blue, red and black, respectively. The tiltograms are for the approaching velocity side of each galaxy; the magenta dashed lines mark r_{warp} , if a warp is present.

Table A2. WISE photometric measurements for the LVHIS galaxies (continued).

IDs	luminosities and colour						structural parameters			
index	log L _{W1} [L _⊙]	L _{W2} [L _⊙]	L _{W3} ¹ [L _⊙]	L _{W4} ¹ [L _⊙]	L _{W1} ² [L _{⊙,W1}]	W1-W2 [mag]	r _s ³ [arcsec]	r _{eff} ⁴ [arcsec]	μ _{eff} ⁴ [mag arcsec ⁻²]	R ₇₅ /R ₂₅ ⁵
76 ^f	6.110±0.048	5.608±0.203	-	-	7.470±0.052	-0.265	32.6	17.2	21.587	2.11
77	8.122±0.011	7.748±0.019	7.506±0.026	7.769±0.029	9.481±0.023	0.059	99.0	93.8	18.584	2.77
78	7.266±0.040	6.911±0.059	6.555±0.049	6.493±0.079	8.625±0.045	0.103	74.3	60.1	18.653	3.02
79	5.823±0.018	5.463±0.043	-	-	7.183±0.027	0.091	55.5	42.9	21.272	2.45
80	6.475±0.015	6.130±0.034	-	-	7.835±0.025	0.129	66.8	52.5	20.794	2.52
81	6.261±0.026	5.827±0.075	-	5.492±0.329	7.620±0.033	-0.092	17.4	15.6	20.520	2.91
82	8.514±0.011	8.153±0.019	8.235±0.014	8.063±0.018	9.873±0.023	0.090	131.5	119.2	18.357	2.61





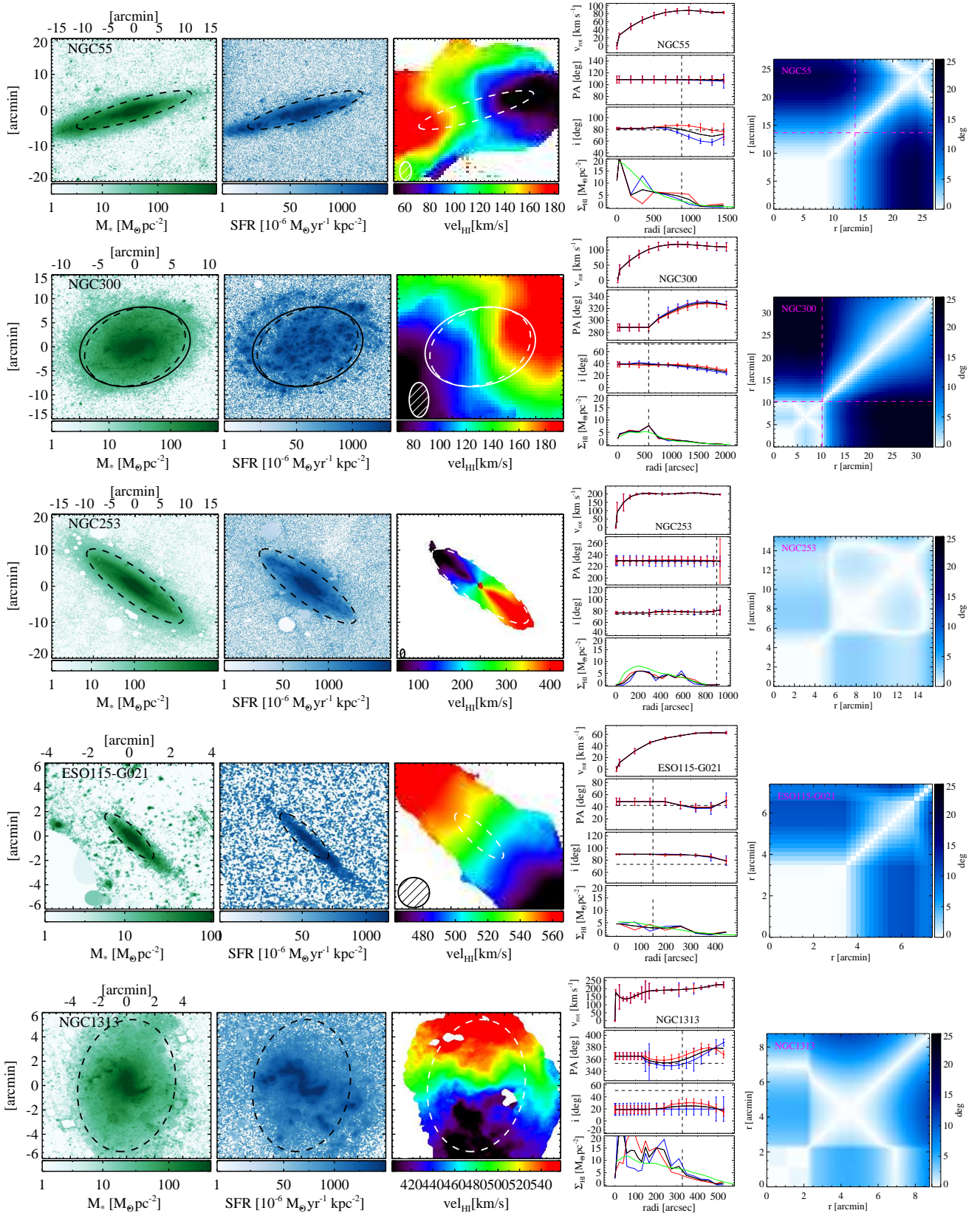


Figure B2. From left to right: distributions of M_* and SFR (at the resolution of the WISE W1- and W4-bands, respectively), mean ATCA HI velocity field at the original resolution, tilted ring models and tiltograms (approaching side) for the same ten large LVHIS galaxies as shown in Figure B1 (See Section B). To be continued.

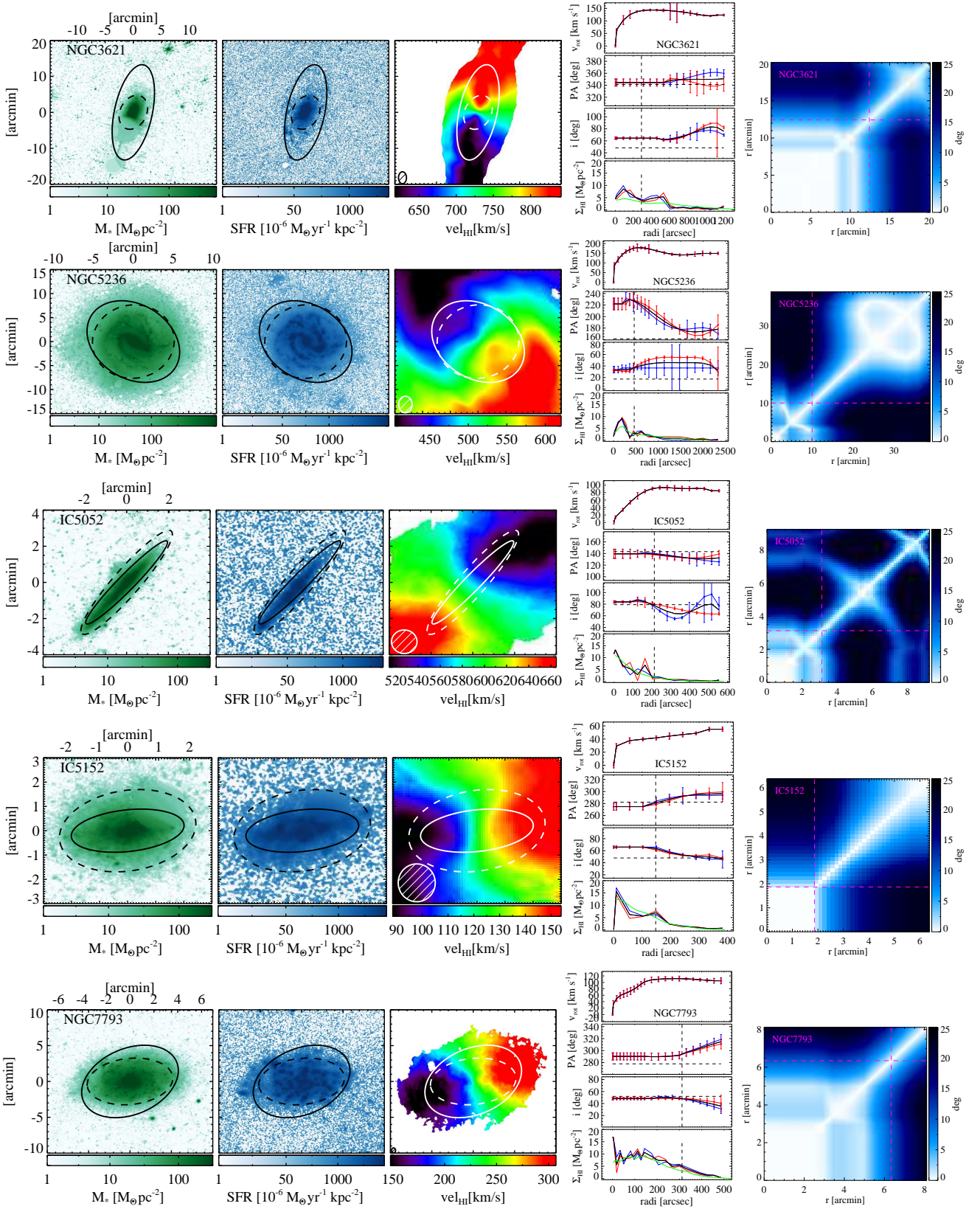


Figure B2. Continued. From left to right: distributions of M_* and SFR (at the resolution of the WISE W1- and W4-bands, respectively), mean ATCA HI velocity field at the original resolution, tilted ring models and tiltograms (approaching side) for the same ten large LVHIS galaxies as shown in Figure B1.